# Mantle melting as a function of water content beneath back-arc basins

Katherine A. Kelley,[1,2,3] Terry Plank,[1] Timothy L. Grove,[4] Edward M. Stolper,[5] Sally Newman,[5] and Erik Hauri[2]

Received 15 March 2005; revised 25 January 2006; accepted 29 March 2006; published 28 September 2006.

[1] Subduction zone magmas are characterized by high concentrations of $H_2O$, presumably derived from the subducted plate and ultimately responsible for melting at this tectonic setting. Previous studies of the role of water during mantle melting beneath back-arc basins found positive correlations between the $H_2O$ concentration of the mantle ($H_2O_o$) and the extent of melting ($F$), in contrast to the negative correlations observed at mid-ocean ridges. Here we examine data compiled from six back-arc basins and three mid-ocean ridge regions. We use $TiO_2$ as a proxy for $F$, then use $F$ to calculate $H_2O_o$ from measured $H_2O$ concentrations of submarine basalts. Back-arc basins record up to 0.5 wt % $H_2O$ or more in their mantle sources and define positive, approximately linear correlations between $H_2O_o$ and $F$ that vary regionally in slope and intercept. Ridge-like mantle potential temperatures at back-arc basins, constrained from Na-Fe systematics (1350°–1500°C), correlate with variations in axial depth and wet melt productivity (~30–80% $F$/wt % $H_2O_o$). Water concentrations in back-arc mantle sources increase toward the trench, and back-arc spreading segments with the highest mean $H_2O_o$ are at anomalously shallow water depths, consistent with increases in crustal thickness and total melt production resulting from high $H_2O$. These results contrast with those from ridges, which record low $H_2O_o$ (<0.05 wt %) and broadly negative correlations between $H_2O_o$ and $F$ that result from purely passive melting and efficient melt focusing, where water and melt distribution are governed by the solid flow field. Back-arc basin spreading combines ridge-like adiabatic melting with nonadiabatic mantle melting paths that may be independent of the solid flow field and derive from the $H_2O$ supply from the subducting plate. These factors combine significant quantitative and qualitative differences in the integrated influence of water on melting phenomena in back-arc basin and mid-ocean ridge settings.

**Citation:** Kelley, K. A., T. Plank, T. L. Grove, E. M. Stolper, S. Newman, and E. Hauri (2006), Mantle melting as a function of water content beneath back-arc basins, *J. Geophys. Res.*, *111*, B09208, doi:10.1029/2005JB003732.

## 1. Introduction

[2] Water has long been understood to play a major role in the generation of subduction zone magmas. In essence, water lowers the mantle solidus [e.g., *Kushiro et al.*, 1968], which ultimately drives melting of the mantle wedge beneath arcs and back-arc basins due to a flux of water originating from the dehydrating, subducting slab. This has been the working paradigm for subduction zone magma genesis for more than 20 years, supported by the widespread observations that subduction zone lavas are vesicular and explosive, contain hydrous phenocrysts [e.g., *Gill*, 1981], follow hydrous liquid lines of descent [*Sisson and Grove*, 1993a], are enriched in fluid-mobile trace elements [e.g., *Morris et al.*, 1990], and carry trace element and isotopic signatures characteristic of subducting sediment and oceanic crust [e.g., *Tera et al.*, 1986; *Plank and Langmuir*, 1993; *Miller et al.*, 1994]. High $H_2O$ concentrations in arc magmas have been inferred or estimated using innovative analytical and experimental techniques, [e.g., *Anderson*, 1979, 1982; *Sisson and Grove*, 1993a, 1993b; *Gaetani et al.*, 1994], and direct measurements of $H_2O$ in submarine glasses and melt inclusions have supported these earlier estimates of dissolved $H_2O$ in arc and back-arc lavas [e.g., *Muenow et al.*, 1980; *Aggrey et al.*, 1988; *Muenow et al.*, 1991; *Danyushevsky et al.*, 1993; *Sisson and Layne*, 1993; *Stolper and Newman*, 1994] (hereinafter referred to as S&N94). Notably, a significant increase in the number of direct measurements of volatile contents in arc and back-arc magmas in recent years [e.g., *Kamenetsky et al.*, 1997; *Roggensack et al.*, 1997; *Sisson and Bronto*, 1998; *Newman et al.*, 2000; *Fretzdorff et al.*,

[1]Department of Earth Sciences, Boston University, Boston, Massachusetts, USA.
[2]Department of Terrestrial Magnetism, Carnegie Institution of Washington, Washington, D. C., USA.
[3]Now at Graduate School of Oceanography, University of Rhode Island, Narragansett, Rhode Island, USA.
[4]Department of Earth, Atmospheric and Planetary Sciences, Massachusetts Institute of Technology, Cambridge, Massachusetts, USA.
[5]Division of Geological and Planetary Sciences, California Institute of Technology, Pasadena, California, USA.


0148-0227/06/2005JB003732$09.00

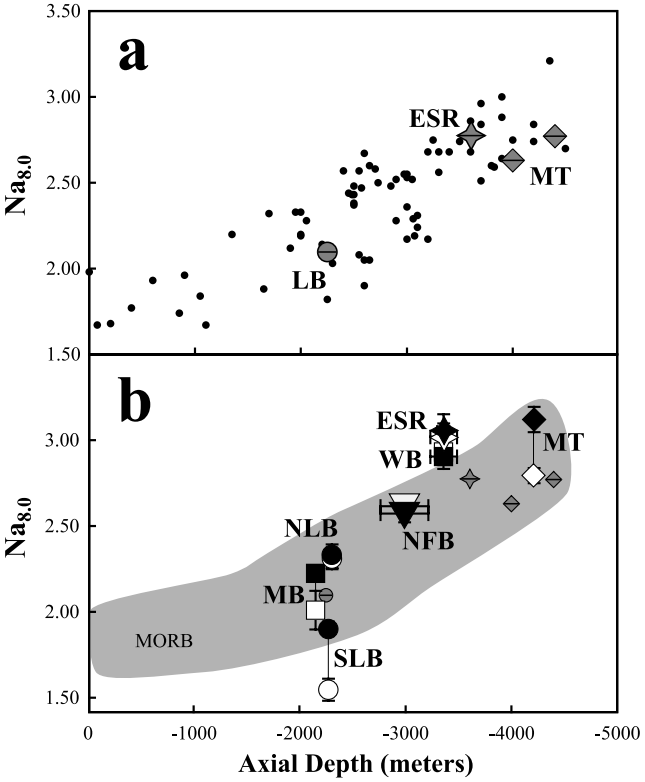


**Figure 1.** $Na_{8.0}$ versus axial depth in global MORB and back-arc basins. (a) MORB and back-arc basin regional averages from *Klein and Langmuir* [1987]. The black circles are MORB, and the barred shaded symbols are back arcs. Abbreviations are as follows: MT, Mariana trough; ESR, East Scotia ridge; LB, Lau basin. *Klein and Langmuir* [1987] reported two values for the Mariana trough at 17.39°N (4000 m depth) and at 18.01°N (4400 m depth). (b) Back-arc basin basalts from the compilation in this study superimposed on the data and trends of *Klein and Langmuir* [1987]. The white symbols are average back arcs (unfiltered for $H_2O$ content (this study, Table 3)), the black symbols are average, dry back-arc basin basalts ($H_2O$ < 0.5 wt % (this study, Table 3)), the barred shaded symbols are back arcs from *Klein and Langmuir* [1987] as in Figure 1a, and the shaded field is the MORB array from Figure 1a. Abbreviations are as follows: WB, Woodlark basin; NFB, North Fiji basin; NLB, northern Lau basin; SLB, southern Lau basin; MB, Manus basin; other abbreviations as in Figure 1a.

2002; *Kent et al.*, 2002; *Cervantes and Wallace*, 2003; *Sinton et al.*, 2003; *Walker et al.*, 2003] has set the stage for a quantitative investigation of water in natural subduction zone settings.

[3] Back-arc basins are natural places to begin such a study because they can be treated, in many ways, like mid-ocean ridges. The driest back-arc basin melts are compositionally equivalent to mid-ocean ridge melts and thus, like mid-ocean ridge magmas, can be interpreted as melts generated by varying extents of adiabatic decompression melting of ascending mantle. For example, the driest back-arc basin basalts overlap with MORBs on $Na_{8.0}$-axial depth plots (Figure 1 [see also *Klein and Langmuir*, 1987]) and plots of $Na_2O$ versus FeO (Figure 2 [see also *Langmuir et al.*, 1992; *Taylor and Martinez*, 2003]). Both inter- and intrabasin systematics of back arcs were recently explored by *Taylor and Martinez* [2003], who compared major and trace element variations (e.g., $Na_{8.0}$, $Fe_{8.0}$, $Ti_{8.0}$, $H_2O_{(8.0)}$, Ba/La) of four back-arc basins to global MORB; their work emphasizes the hybrid nature of the back-arc basin melting process, identifying MORB-like geochemical systematics in relatively dry back-arc melts and showing how these systematics are perturbed in wetter samples by the addition of $H_2O$-rich material from the subducted slab. The melting process in back arcs is also not complicated, as it may be in arcs, by the effects of overlying crust, since crustal assimilation is a small concern and crustal thickness will not impact the melting column because it is a passive consequence of melting just as at ridges. Additionally, back arcs are less subject to the thermal influence of the cold subducting slab, and may reflect ambient upper mantle temperature variations as ridges do. Back-arc basins are therefore potentially ideal sites for studying the effects of variations in mantle temperature and water contents on mantle melting with fewer complicating factors than arcs.

[4] The quantitative relationship between water and mantle melting over the range of tectonic settings has been investigated in only a few localities, with contrasting results. S&N94 evaluated the importance of water in the formation of magmas at the Mariana trough back-arc spreading center

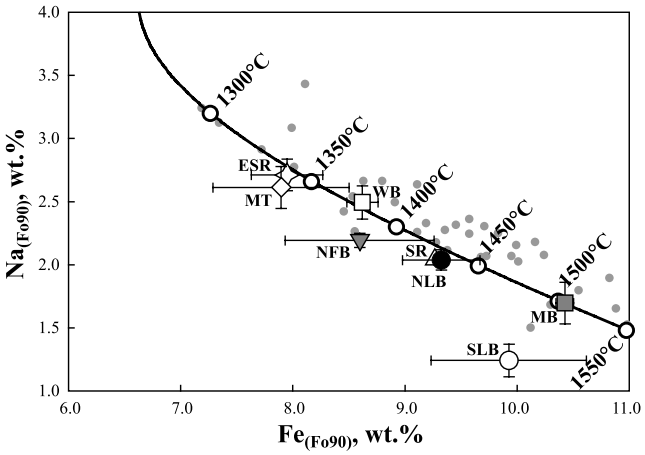


**Figure 2.** Regionally averaged $Na_{(Fo90)}$ versus $Fe_{(Fo90)}$ in MORB and back-arc basin basalts ($Na_2O$ and FeO concentrations corrected to equilibrium with $Fo_{90}$; see section 2). The shaded points are MORB from *Langmuir et al.* [1992]. The black line connected by open circles shows the MORB model curve with potential temperatures from *Langmuir et al.* [1992]. Symbols are averages of the driest back-arc basin basalts from each region (<0.5 wt % $H_2O$; same as solid symbols in Figure 1b and Table 3); the open diamond is the Mariana trough (MT); the open star is the East Scotia ridge (ESR); the open square is the Woodlark basin (WB); the shaded inverted triangle is the North Fiji basin (NFB); the open triangle is the Sumisu rift (SR); the solid circle is the northern Lau basin (NLB); the open circle is the southern Lau basin (SLB); and the shaded square is the Manus basin (MB). The Sumisu rift and southern Lau basin contain no dry basalts, but average data for these regions are shown for reference.

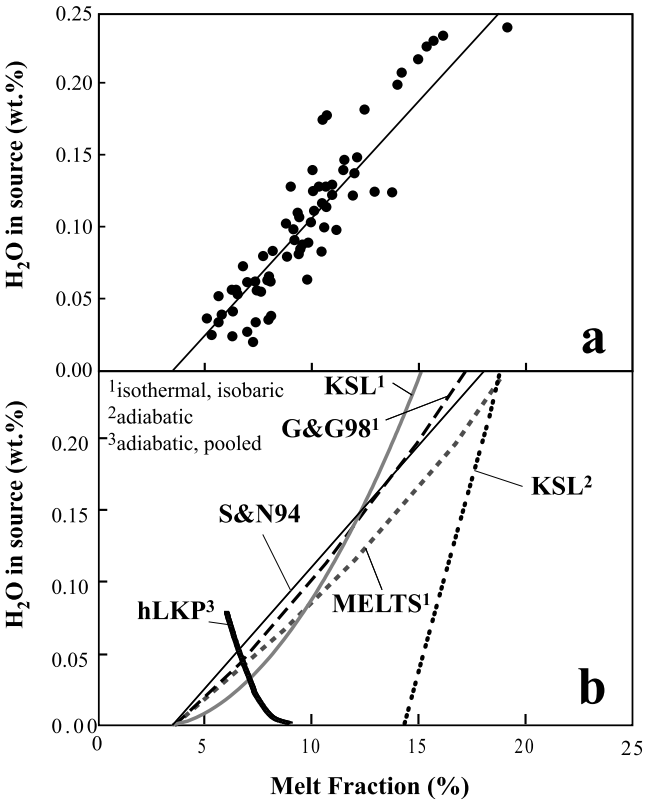


**Figure 3.** $H_2O_o$ versus $F$ from the literature. (a) Original figure from S&N94 showing their Mariana trough data and the linear best fit. (b) Models compiled from the literature for wet melting of peridotite. The thin, solid black line (S&N94) is the S&N94 Mariana trough best fit line from Figure 3a; the thick, short-dashed, shaded line (MELTS) is the isobaric, isothermal MELTS calculation from *Hirschmann et al.* [1999] at 1350°C and 1 GPa; the thin, long-dashed, black line (G&G98) is the fit to the isobaric, isothermal experimental results from G&G98 at 1350°C and 1.5 GPa; the triple-dotted black line ($KSL^2$) is an adiabatic model result of *Katz et al.* [2003] for $T_p$ = 1250°C; the solid shaded line ($KSL^1$) is an isobaric, isothermal model result from *Katz et al.* [2003] at 1250°C and 1 GPa; the bold black line (hLKP) is an adiabatic model result from *Asimow and Langmuir* [2003] for $T_p$ = 1350°C, pooled from a 2-D melting triangle.

using concentrations of volatile, major, and trace elements from submarine glasses. This work was the first to recognize correlations between trace elements and water contents of subduction-related lavas and suggested a positive, roughly linear relationship between the extent of mantle melting (i.e., melt fraction; $F$) and the $H_2O$ concentration of the mantle (Figure 3a). The basis for pure "flux melting" models originates from this study. Correlations between $H_2O$ and trace elements in volcanic arc melts [e.g., *Grove et al.*, 2002; *Cervantes and Wallace*, 2003; *Walker et al.*, 2003] provide supporting evidence for the importance of the flux melting mechanism beneath arcs, although nominally dry arc melts from Japan [*Tatsumi et al.*, 1983], the Cascades [*Bartels et al.*, 1991], and Java [*Sisson and Bronto*, 1998] implicate mantle decompression as another means of melt generation beneath arcs. In contrast to the positive correlation between $H_2O$ and $F$ described or inferred for back-arc basin and arc lavas, recent models of hot spot-influenced, "damp" mid-ocean ridges [*Detrick et al.*, 2002; *Asimow et al.*, 2004; *Cushman et al.*, 2004] suggest a negative correlation between $H_2O$ and $F$ (e.g., Figure 3b, hLKP curve). The differences in the relationships between water content and extent of melting in two such similar tectonic settings as back-arc basins and mid-ocean ridges present a dilemma that we address in this study.

[5] Theoretical, empirical, and experimental investigations of the role of water in mantle melting underscore the differences observed in natural settings. For example, experimental work [*Gaetani and Grove*, 1998] (hereinafter referred to as G&G98), thermodynamic modeling [*Hirschmann et al.*, 1999], and empirical parameterizations of experimental and thermodynamic data [*Katz et al.*, 2003] have shown that the positive melting trend observed in the Mariana trough is readily reproduced through isothermal, isobaric equilibration of fertile mantle with increasing $H_2O$ content (Figure 3b, MELTS, G&G98, and $KSL^1$ curves), although such conditions do not translate easily into a physical melting process in the earth [S&N94; *Hirschmann et al.*, 1999; *Asimow and Langmuir*, 2003]. Parameters such as temperature and pressure certainly vary in natural systems, and the apparent similarities between these studies and the Mariana trough trend may indeed be only coincidental. On the other hand, *Asimow and Langmuir* [2003] used simple thermodynamic models to propose that adding water to decompression melting regimes at mid-ocean ridges will, seemingly paradoxically, increase total melt production but simultaneously decrease the mean extent of melting. This situation arises when pooling melts from a two-dimensional (2-D) triangular melting regime because low-$F$, wet melts originate from the large source volume at the triangle's base. Such a geometry can thus lead to a decrease in mean $F$ with increasing $H_2O$ in the mantle (Figure 3b, hLKP curve). Although this effect has been documented at hot spot-influenced mid-ocean ridges [*Detrick et al.*, 2002; *Asimow et al.*, 2004; *Cushman et al.*, 2004], it has not been seen in the high-$H_2O$ lavas from back-arc basins. *Katz et al.* [2003] also developed an empirical parameterization of hydrous, adiabatic melting. The relationship between $H_2O$ content and extent of melting in their hydrous, adiabatic melting model, however, contrasts with both the observed trend in the Mariana trough and with other efforts to model hydrous, adiabatic melting (Figure 3b, $KSL^2$ curve). Their model produces positive correlations between $H_2O$ in the source and $F$, but the steepness of the trend suggests that $H_2O$ addition does not lead to a significant increase in extent of melting, and thus that $H_2O$-fluxed melting contributes volumetrically very little to the final melt produced by adiabatic decompression in this model. For back-arc basins, therefore, we must presently choose between, on the one hand, an unlikely melting process (i.e., flux-induced, isothermal, isobaric melting) that produces trends similar to those observed in nature or, on the other hand, an apparently more realistic melting process (i.e., polybaric, hydrous, adiabatic melting) for which current models do not reproduce observed trends.

[6] In the work reported in this paper, we studied aspects of the differences between ridge and back-arc melting

systematics, focusing in particular on discriminating between the competing effects of $H_2O$, decompression, and mantle temperature on melt production. Using available measurements of the water contents of glasses from several back-arc basins, we first show that the positive $H_2O$-$F$ trend of the Mariana trough found by S&N94 is a general phenomenon in back-arc basin settings. In detail, however, these trends differ in important ways from one back-arc region to another. We then use these differences and their correlations with other geochemical and geophysical parameters and the contrasts with comparable data from mid-ocean ridge basalts to demonstrate the unique way in which water drives melting beneath back-arc spreading centers.

## 2. Methods and Data Treatment

[7] In order to test the competing models of wet melting, we must be able to determine and compare the extent of mantle melting ($F$) and the concentration of $H_2O$ in the mantle ($H_2O_o$) over a broad range of mid-ocean ridge and back-arc basin basalt compositions. Here, we present the methods we used to filter and correct the data, to calculate $F$ and $H_2O_o$, and to estimate other relevant factors such as mantle potential temperature ($T_p$), axial depth, and crustal thickness in a self-consistent manner. Readers more interested in an outline of the methodology than in the details may skip to the methods summary presented in section 2.8.

### 2.1. Back-Arc Basin Basalt Data

[8] We compiled a global data set of major element and volatile measurements for 408 glasses and olivine-hosted melt inclusions from six back-arc basin localities (Mariana trough [*Volpe et al.*, 1987; *Hawkins et al.*, 1990; S&N94; *Gribble et al.*, 1996, 1998; *Newman et al.*, 2000], Sumisu rift [*Hochstaedter et al.*, 1990a], Manus basin [*Danyushevsky et al.*, 1993; *Kamenetsky et al.*, 2001; *Sinton et al.*, 2003; *Shaw et al.*, 2004], North Fiji basin [*Aggrey et al.*, 1988; *Danyushevsky et al.*, 1993], Lau basin [*Aggrey et al.*, 1988; *Danyushevsky et al.*, 1993; *Sinton et al.*, 1993; *Pearce et al.*, 1995; *Kamenetsky et al.*, 1997; *Peate et al.*, 2001; *Kent et al.*, 2002; A. J. Kent, unpublished data, 2002; S. Newman, unpublished data, 1994] and East Scotia ridge [*Muenow et al.*, 1980; *Leat et al.*, 2000; *Fretzdorff et al.*, 2002; *Newman and Stolper*, 1995; S. Newman, unpublished data, 2002]) and three mid-ocean ridge and ridge-like regions (Galápagos spreading center [*Cushman et al.*, 2004], Mid-Atlantic Ridge and Azores platform [*Dixon et al.*, 2002], and Woodlark basin [*Muenow et al.*, 1991; *Danyushevsky et al.*, 1993]).

[9] Before using these data to model $F$ and $H_2O_o$, we first considered how the composition of each glass may have changed through degassing and crystal fractionation. To assess how degassing may have affected $H_2O$, we examined another volatile species, $CO_2$, which has much lower solubility than $H_2O$ in silicate melt and degasses nearly to completion before $H_2O$ degassing initiates during open system degassing [*Dixon et al.*, 1995]. The presence of measurable $CO_2$ is thus an indicator that $H_2O$ has likely not been significantly affected by degassing, but $CO_2$ data are not published for many of the samples used in this study. The combined concentrations of $H_2O$ and $CO_2$ in a melt, however, are pressure sensitive and, in submarine lavas, usually reflect vapor saturation or supersaturation at or near the hydrostatic pressure of eruption [*Dixon and Stolper*, 1995]. We thus calculated the saturation pressure of each sample with respect to pure $H_2O$ (i.e., $CO_2$ = 0 ppm). Glasses with pure $H_2O$ saturation pressures equal to or greater than their collection depths probably reached saturation with $H_2O$ vapor and experienced some $H_2O$ degassing. To account for uncertainties in eruption/collection depth and the chance that lava flowed downhill from the eruption site, we included only those samples with pure $H_2O$ saturation pressures at least 30 bars less than the pressure at the collection depth. Exceptions to these criteria were made in the case of basaltic melt inclusions, which are often trapped at high pressure within the magma chamber and, if $H_2O$ concentrations are high (e.g., at the Valu Fa ridge), may record $H_2O$ saturation pressures much higher than those at the sample collection depth. In these cases, only melts with measured $CO_2$ concentrations >30 ppm were considered undegassed.

[10] To compensate for the effects of crystal fractionation, all samples that were determined to have escaped significant $H_2O$ degassing were back corrected to primary mantle melts using several steps. The regional data sets were first filtered to exclude all glasses with MgO < 7 wt %, in order to eliminate highly fractionated compositions. One exception to this criterion was made in the case of the Manus basin, where basalt compositions with MgO $\geq$ 6.25 wt % were included in order to allow a greater number of samples to represent this region. Of the remaining samples, those with MgO < 8 wt % were corrected to 8 wt % MgO using the $Fe_{8.0}$ and $Na_{8.0}$ expressions from *Klein and Langmuir* [1987] and the $TiO_{2(8.0)}$ and $H_2O_{(8.0)}$ expressions from *Taylor and Martinez* [2003]:

$$Fe_{8.0} = FeO - 1.66 \times (8.0 - MgO), \quad (1)$$

$$Na_{8.0} = Na_2O - 0.373 \times (8.0 - MgO), \quad (2)$$

$$TiO_{2(8.0)} = TiO_2 \times MgO^{1.7}/8.0^{1.7}, \quad (3)$$

$$H_2O_{(8.0)} = H_2O \times MgO^{1.7}/8.0^{1.7}. \quad (4)$$

We then employed an additional fractionation correction to 8.5 wt % MgO because most melts are still on olivine + plagioclase cotectics at 8 wt % MgO and adding olivine only (see below) at this point leads to false high Fe. The fractionation slopes for this step are shallower than those above, but consistent with olivine + plag cotectic slopes predicted by the liquid line of descent algorithm of *Weaver and Langmuir* [1990]:

$$Fe_{8.5} = Fe_{8.0} - 1.2 \times (8.5 - 8.0), \quad (5)$$

$$Na_{8.5} = Na_{8.0} - 0.135 \times (8.5 - 8.0), \quad (6)$$

$$TiO_{2(8.5)} = TiO_{2(8.0)} - 0.3 \times (8.5 - 8.0), \quad (7)$$

$$H_2O_{(8.5)} = H_2O_{(8.0)} - 0.05 \times (8.5 - 8.0). \quad (8)$$

Glasses with initial MgO between 8.0 and 8.5 wt % were corrected to 8.5 wt % MgO only along these linear ol + plag cotectics by substituting the measured glass concentrations of FeO, $Na_2O$, $TiO_2$ and $H_2O$ for $Fe_{8.0}$, $Na_{8.0}$, $TiO_{2(8.0)}$ and $H_2O_{(8.0)}$ and substituting the measured concentration of MgO for the 8.0 term inside the parentheses in equations (5), (6), (7), and (8). We then back corrected these 8.5% MgO-equivalent compositions, as well as all glasses with initial MgO $\geq$ 8.5 wt % (to which no correction had yet been applied), to primary mantle melts by adding equilibrium olivine (using $K_D^{ol\text{-}liq}$[Mg – Fe] = 0.3) to each glass composition in 1% increments until in equilibrium with $Fo_{90}$ (as in the work of S&N94). These corrected liquid compositions provide $Fe_{(Fo90)}$ and $Na_{(Fo90)}$, which are discussed throughout and are used to calculate mantle potential temperature (see section 2.7), and $C^l_{Ti}$ and $C^l_{H_2O}$ (i.e., $TiO_{2(Fo90)}$ and $H_2O_{(Fo90)}$), which are input to equations (9) and (10) below. Most samples required $\leq$15% olivine addition to reach $Fo_{90}$ equilibrium, but to avoid artifacts from overcorrection, the few samples requiring >30% olivine addition were excluded. These three criteria (degassing, MgO content, and fractionation) are the only constraints used to filter the data; ~50% of the original data compilation ($n$ = 224) passed the filter and were used for the modeling.

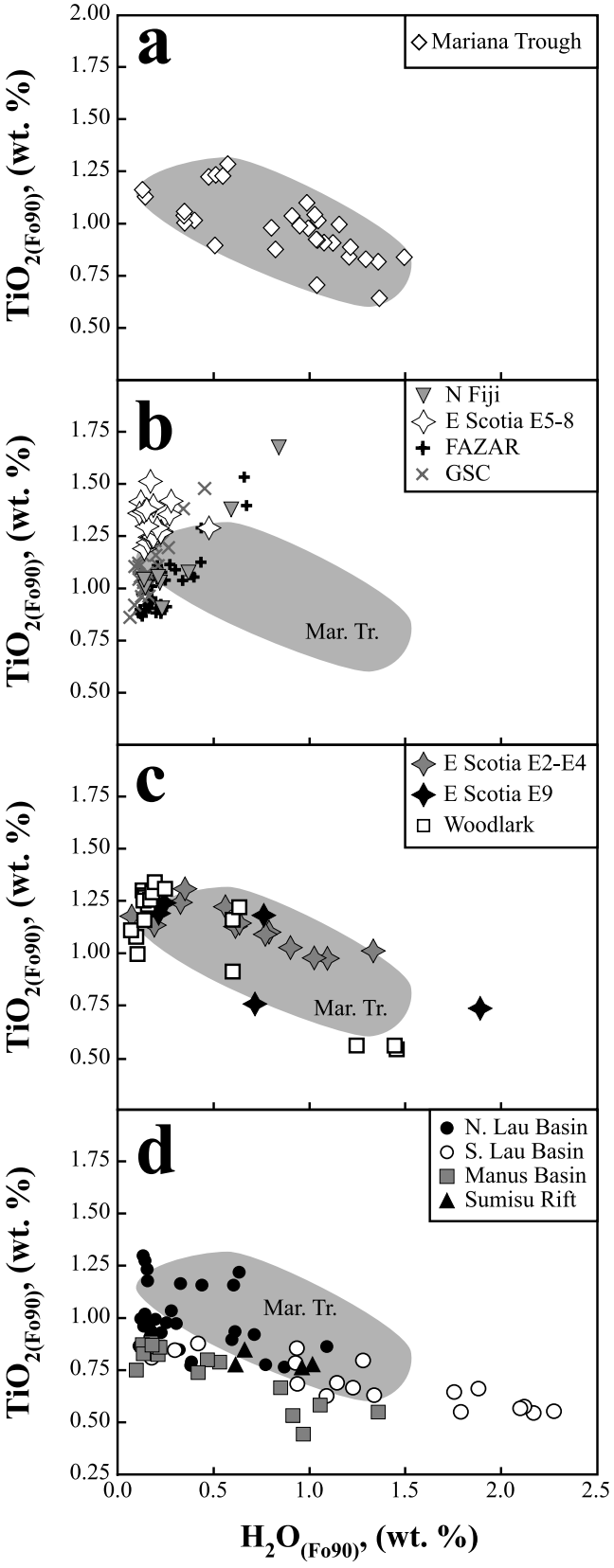


**Figure 4.** $TiO_2$ versus $H_2O$ in back-arc basin basalts, calculated to equilibrium with $Fo_{90}$ (see text): (a) Mariana trough (after S&N94); (b) mid-ocean ridges (Mid-Atlantic Ridge (FAZAR), Galápagos spreading center (GSC)) and back-arc basin segments (North Fiji basin, East Scotia ridge E5–E8) showing positive correlations; (c) mid-ocean ridge (Woodlark basin) and back-arc basin segments (East Scotia ridge E2–E4 and E9) showing both negative and positive correlations; and (d) back-arc basin segments showing negative correlations (northern and southern Lau basin, Manus basin, Sumisu rift).

### 2.2. Modeling Mantle Melt Fractions and Water Contents of Mantle Sources

[11] S&N94 performed a multielement inversion on a suite of Mariana trough glasses to constrain melt fraction and source composition. This inversion was based on the simplifying assumption that variations in Mariana trough basalt chemistry reflect variable extents of melting correlated with mixing of two source components: one similar to the mantle source of normal mid-ocean ridge basalt (NMORB) and the other a water-rich component derived from the subducted slab. They chose the most MORB-like basalt composition and assumed it reflected 5% batch melting of unmodified NMORB source to obtain the composition of this source component. They then used an iterative procedure based on the $H_2O$, $TiO_2$, $K_2O$, $Na_2O$, and $P_2O_5$ contents of each glass to solve simultaneously for the composition of the $H_2O$-rich component, the fraction of this component in the source of each sample, and the extent of melting of the source by which each sample was produced. Although this method succeeds for the Mariana trough, the assumptions (1) of a two-component system (requiring that enough data exist to define clear mixing relationships and that additional components are not involved), (2) of a $H_2O$-poor NMORB mantle source and a $H_2O$-rich component that are constant in composition, and (3) of 5% melting to produce the NMORB end-member

**Table 1.** Mantle Source Constraints for Back-Arc Basins and Ridges

| Basin | Region/Segment | Source Model[a] | *f* Removed, % | $C^{o}_{Ti}$ | +[b] | −[b] |
|---|---|---|---|---|---|---|
| Mariana trough | | DMM | 0 | 0.133 | 0.000 | 0.012 |
| Sumisu rift | | DMM | 0.10 | 0.130 | 0.003 | 0.003 |
| Lau basin | CLSC | DMM | 1.00 | 0.107 | 0.014 | 0.002 |
| | ELSC-VFR | DMM | 2.50 | 0.083 | 0.024 | 0.006 |
| | ILSC | DMM | 0 | 0.133 | 0.000 | 0.003 |
| | MTJ | DMM | 0 | 0.133 | 0.000 | 0.003 |
| Manus basin | MSC | DMM | 0.80 | 0.112 | 0.015 | 0.005 |
| | ETZ | DMM | 0.80 | 0.112 | 0.015 | 0.005 |
| | ER | DMM | 0.15 | 0.128 | 0.005 | 0.004 |
| | SR | DMM | 0.80 | 0.112 | 0.015 | 0.005 |
| East Scotia ridge | E2–E4 | DMM | 0 | 0.133 | 0.000 | 0.006 |
| | E5–E6 | DMM | 0.15 | 0.128 | 0.005 | 0.004 |
| | E7–E8 | DMM | 0.40 | 0.121 | 0.006 | 0.005 |
| | E9 | Ti/Y | ... | 0.192 | 0.007 | 0.007 |
| North Fiji basin | TJ | Ti/Y | ... | 0.151 | 0.012 | 0.012 |
| | N160° | Ti/Y | ... | 0.198 | 0.024 | 0.024 |
| Woodlark basin | west/D'Entrecasteaux | Ti/Y | ... | 0.172 | 0.013 | 0.013 |
| | center | DMM | 0.50 | 0.119 | 0.014 | 0.003 |
| | east | DMM | 0.40 | 0.121 | 0.012 | 0.005 |
| | northeast | DMM | 0.10 | 0.130 | 0.003 | 0.003 |
| GSC | E | *Cushman et al.* [2004] | ... | 0.143 | ... | ... |
| | T | *Cushman et al.* [2004] | ... | 0.108 | ... | ... |
| | N | *Cushman et al.* [2004] | ... | 0.105 | ... | ... |
| Azores | KP | Ti/Y | ... | 0.189 | 0.014 | 0.014 |
| | PO | Ti/Y | ... | 0.143 | 0.002 | 0.002 |
| | OH | Ti/Y | ... | 0.139 | 0.003 | 0.003 |
| | HA | Ti/Y | ... | 0.137 | 0.003 | 0.003 |

[a]DMM source model denotes the use of prior melt extraction to constrain source variation. Ti/Y source model denotes cases where the mantle source is enriched, and the $TiO_2$/Y model is used to constrain source characteristics.
[b]Columns denote errors on the value of $C^{o}_{Ti}$.

may not apply to other regions. An alternative approach is therefore necessary because, in many regions, data sets are limited, the compositions of the mantle source and/or slab-derived component may vary regionally, and the extent of melting of the MORB-like end-member is unlikely to be constant for all back arcs.

[12] Rather than performing a best fit based on several relatively incompatible elements (including some likely present in significant concentrations in the slab-derived components) to constrain $F$ for each sample, we used $TiO_2$ in glasses as a single-element proxy for melt fraction ($F$). Like any other element that is incompatible during mantle melting, $TiO_2$ decreases monotonically in the melt with increasing $F$ of a single source. While it is difficult to identify a truly "conservative" element in subduction zones (i.e., an element not added from the subducted slab [*Pearce and Parkinson*, 1993]), $TiO_2$ holds promise in this regard because of its low overall abundance in arc lavas and the possibility that it, like other high field strength elements, may be retained in residual rutile in the slab during dehydration [e.g., *Ryerson and Watson*, 1987]. We thus adopted the approximation that, except for dilution, the $TiO_2$ content of sources in a given mantle wedge are independent of the amount of slab-derived component they contain. Moreover, systematics of Mariana trough basalts are consistent with low $TiO_2$ in the $H_2O$-rich component (S&N94), as the data show that increasing $H_2O$ concentrations correlate with decreasing $TiO_2$ and, by proxy, increasing $F$ (Figure 4a (see also S&N94). This correlation is the starting point of the linear wet melting function and was indeed the observation that led S&N94 to first suspect a positive correlation between the water content and melt fraction of the source of Mariana trough lavas.

[13] On the basis of this observation for the Mariana trough (Figure 4a), we used $TiO_2$ to calculate $F$ for all the filtered and corrected back-arc basin basalt and MORB data. To model $F$, the fraction of melting, we solved the batch melting equation to yield

$$F = \frac{\left(C^{o}_{Ti}/C^{l}_{Ti}\right) - D_{Ti}}{(1 - D_{Ti})}, \tag{9}$$

where $C^{o}_{Ti}$ is the concentration of $TiO_2$ in the mantle source (Table 1; see sections 2.4–2.5), $C^{l}_{Ti}$ is the concentration of $TiO_2$ in the melt in equilibrium with $Fo_{90}$ (from basalt data, see section 2.1), and $D_{Ti}$ is the bulk distribution coefficient for Ti during mantle melting (Table 2; see section 2.3). To obtain the concentration of $H_2O$ in the source, we re-solved this equation in terms of $H_2O$ to yield

$$C^{o}_{H_2O} = C^{l}_{H_2O}[F(1 - D_{H_2O}) + D_{H_2O}], \tag{10}$$

where $C^{o}_{H_2O}$ is the concentration of $H_2O$ in the mantle source (hereinafter referred to as $H_2O_o$), $C^{l}_{H_2O}$ is the concentration of $H_2O$ in the melt in equilibrium with $Fo_{90}$ (from basalt data, see section 2.1), $F$ is the output of equation (9), and $D_{H_2O}$ is the bulk distribution coefficient

**Table 2.** Mantle/Melt Partition Coefficients and Starting Composition

| Element | D (Mantle/Melt) | DMM[a] |
|---|---|---|
| Th, ppm | 0.0015 | 0.0137 |
| Nb, ppm | 0.003 | 0.21 |
| Ta, ppm | 0.005 | 0.0138 |
| La, ppm | 0.0075 | 0.234 |
| Ce, ppm | 0.011 | 0.772 |
| $H_2O$, ppm | 0.012 | 116 |
| Pr, ppm | 0.015 | 0.131 |
| Nd, ppm | 0.02 | 0.713 |
| Sm, ppm | 0.03 | 0.27 |
| Zr, ppm | 0.03 | 7.94 |
| Eu, ppm | 0.035 | 0.107 |
| Gd, ppm | 0.04 | 0.395 |
| $TiO_2$, wt % | 0.04 | 0.133 |
| Tb, ppm | 0.048 | 0.075 |
| Dy, ppm | 0.06 | 0.531 |
| Ho, ppm | 0.07 | 0.122 |
| Er, ppm | 0.08 | 0.371 |
| Yb, ppm | 0.095 | 0.401 |
| Y, ppm | 0.095 | 4.07 |
| Lu, ppm | 0.105 | 0.063 |

[a]Depleted MORB mantle composition from *Salters and Stracke* [2004].

for $H_2O$ during mantle melting (from S&N94; see Table 2 and section 2.3).

[14] While end-member batch melting is probably not a realistic melting process, it is a useful approximation for determining the bulk $F$ of basaltic partial melts of the mantle. For example, equation (9) provides a fair approximation of the bulk melt fraction (as reflected in incompatible element concentrations) at mid-ocean ridges despite the likely complexity of the melting regime and melting process in this environment [*Plank and Langmuir*, 1992; *Plank et al.*, 1995]. As a relevant example, the $Na_{8.0}$ and $Ti_{8.0}$ variations in mid-ocean ridge basalts are well described by pooling of melts produced by polybaric, adiabatic, fractional melting with $D$s that vary as a function of pressure, temperature, composition, and mode (Figure 5 [see also *Langmuir et al.*, 1992]). The $Na_{8.0}$-$Ti_{8.0}$ trend, however, is also adequately reproduced with the simplest model (batch melting with constant $C^o$ and $D$s (Figure 5)). Since back arcs tap mantle similar to MORB, and because we know less about the melting process in these settings, we adopted this simple model as our starting point.

### 2.3. Partition Coefficients

[15] The partition coefficients used in the batch melting model impact the results of these calculations. The $D_{Ti}$ used here derives from the simplified MORB model above (Figure 5) and describes partitioning between melt and lherzolitic mantle. Published mantle/melt $D$s for Ti range up to 0.11 [*Kelemen et al.*, 1993], but a value this high is not permitted in the batch melting model, as it produces negative values for $F$ in high-Ti samples. The value used here (0.04) reflects an average $D_{Ti}$ within the range predicted for appropriate variations in pressure, temperature, and melt composition along a polybaric path (e.g., 0.01–0.06 [*Langmuir et al.*, 1992]; <0.01–0.08 [*Baker et al.*, 1995]), and we assess the effect of this uncertainty on the calculations below. In rare cases, extents of melting predicted by the batch melting model exceed 20%. At such high melt fractions, one might expect clinopyroxene (cpx) to become exhausted from the mantle, and the liquid to instead reflect equilibrium partitioning between melt and a two-phase harzburgitic mantle. For the few back-arc samples where cpx may have been exhausted from the mantle (e.g., the Manus basin, based on $CaO/Al_2O_3$), we selected a harzburgite/melt $D_{Ti}$ of 0.05 (average of $D$s reported by *Grove et al.* [2002], *Pearce and Parkinson* [1993], and *Kelemen et al.* [1993]). Because this $D$ is similar to the lherzolite $D$, the change has a small effect on the calculated $F$ and $H_2O_o$. The $D_{H_2O}$ used here (0.012) is adopted from S&N94 in order to be consistent with that study. The value is similar to that for the LREE, consistent with variations observed in MORB [*Michael*, 1988; *Dixon et al.*, 2002]. We evaluate the effect of lowering $D_{H_2O}$ in section 2.6 below.

### 2.4. Modeling Depleted Mantle Source Compositions

[16] The composition of the depleted mantle end-member in the sources of back-arc basin magmas is crucial to the model results, and so we carefully consider here the likely variation of $C^o_{Ti}$ in global back-arc basin and ridge regions. Two variables primarily control the $TiO_2$ concentration of a partial melt of mantle peridotite: the initial concentration of $TiO_2$ in the peridotite and the melt fraction. So while *Taylor and Martinez* [2003] attribute $TiO_2$ variations in back-arc basins largely to variations in source composition, variations in $F$ would also lead to $TiO_2$ variations for a constant source composition, and the challenge is to distinguish whether a melt with low $TiO_2$ reflects high $F$, or a highly depleted mantle, or both. The key to doing so is to use not just $TiO_2$, but several elements with different $D$s during mantle melting; i.e., although the concentration of a single element in a melt can be modeled by an infinite number of combinations of source concentration and $F$, the relative abundances of elements with differing mantle/melt $D$s can

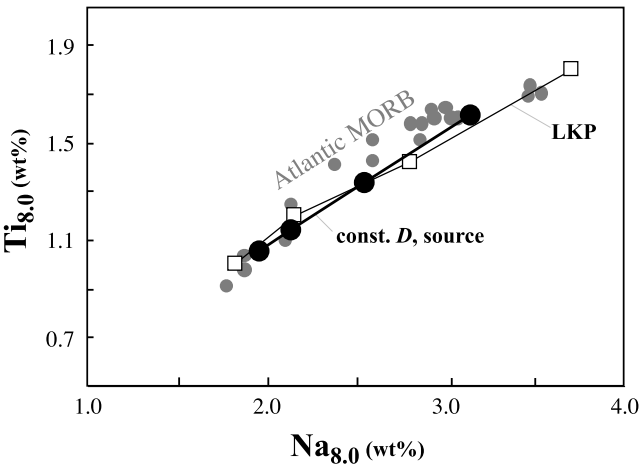


**Figure 5.** $Ti_{8.0}$ versus $Na_{8.0}$ in North Atlantic MORB (shaded circles [*Langmuir et al.*, 1992]) with model fits to the data trend. The thin black line with open squares (LKP) is a polybaric, adiabatic, fractional, pooled melting model, with $D$s varying as a function of pressure, temperature, composition, and mode (taken from *Langmuir et al.* [1992, Figure 55]). The bold line with solid circles (const. $D$, this study) is batch melting with constant $D$s ($D_{Na}$ = 0.02, $D_{Ti}$ = 0.04) and constant mantle source ($C^o_{Na}$ = 0.29 wt %, $C^o_{Ti}$ = 0.133 wt %).

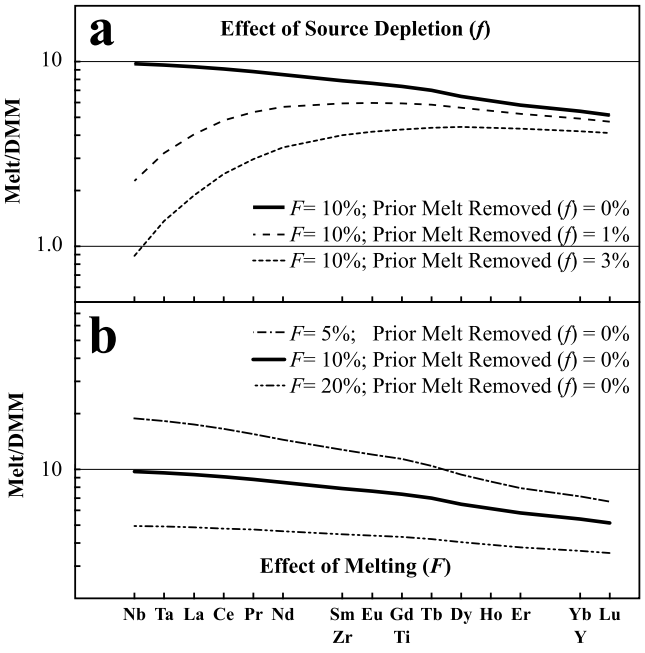


**Figure 6.** Model melt trace element compositions normalized to DMM of *Salters and Stracke* [2004]. (a) Illustrating the effect of mantle source variation on the shape and position of the trace element pattern, keeping $F$ constant at 10%. The curves show the effects of 0, 1, and 3% prior batch melt removal from source on the shape of the pattern. (b) Illustrating the effect of variable melt fraction on the shape and position of the trace element pattern, keeping source concentrations constant (at DMM (Table 2)). Curves show 5, 10, and 20% batch melts of unmodified DMM, using $D$s as in Table 2.

distinguish variations in source composition from variations due to differing extents of melting. For example, source depletion affects highly incompatible elements (e.g., Nb) more than moderately incompatible elements (e.g., Ti (Figure 6a)), while high degrees of melting will affect both elements almost equally provided $F \gg D$ (Figure 6b). Here, we attempt to account for $TiO_2$ variations in mantle sources using a model based on the systematic variations of a suite of elements in lavas from each basin.

[17] A complicating factor in separating variations in the MORB-like mantle composition from variations in extent of melting at subduction zones is that there are probably no elements in the mantle wedge that are completely unaffected by the mass flux from the subducting slab. Nevertheless, for back-arc basin lavas, we will assume most trace element enrichments (e.g., LREE) are additions from the slab-derived, $H_2O$-rich component, whereas incompatible element depletion is a feature of the MORB-like mantle. We therefore chose several relatively conservative elements, spanning a range of mantle/melt $D$s (Y, Ti, Zr, Nb, and Ta) to set constraints on mantle source variations. These high field strength elements vary systematically during mantle melting at mid-ocean ridges and, unlike the light rare earth elements and Th, are expected to be retained in the slab by residual rutile [*Pearce and Parkinson*, 1993]. These are thus among the elements in the mantle least affected by addition of slab-derived components.

[18] Figure 7 illustrates how we determined the composition of the end-member mantle sources for the back-arc spreading centers, to ultimately derive $C^o_{Ti}$. We did this by fitting the conservative element pattern (rather than the full trace element pattern, most of which is sensitive to slab additions (e.g., Figure 7)) of natural lava samples with a melt removal model to determine the source composition of the ''slab-free'' mantle end-member for each basin or subregion within a basin. Mantle source variation is expressed as a function of prior melt removal from an average mantle composition. We chose as the starting point the depleted MORB mantle (DMM) composition of *Salters and Stracke* [2004], which represents an average composition of the mantle that provides the source of MORB. The melt removal model controls the trace element characteristics of the mantle source by removing a specified fraction of melt ($f$) from DMM using batch melting and the bulk mantle/melt $D$s in Table 2. That is, $f$ represents a melt fraction that has been removed from the mantle prior to the melting that takes place within the ridge or back-arc magma source. The removal of $f$ creates depletion of the mantle before it enters into the ridge and back-arc sources. Subsequent melting of these depleted sources, which is the melting step that generates mid-ocean ridge and back-arc basin magmas ($F$, as defined in section 2.2), employs these same $D$s. Source depletion (the removal of $f$ from DMM) has a large effect on the shape of the trace element pattern of a melt (Figure 6a), whereas $F$ controls the absolute abundances of all elements, shifting the whole pattern up or down with a minimal effect on shape (Figure 6b), because $f$ is usually a small value (<3%) and $F$ is a large value (typically 10–20%) with respect to the $D$s modeled. Prior melt removal ($f$) has the largest effect on the most incom-

**Figure 7.** Trace element models constraining mantle source characteristics for basins and segments with depleted mantle sources (equal to or more depleted than DMM), normalized to DMM of *Salters and Stracke* [2004]. Figures for each region are split between two panels. Top panels show complete trace element patterns for two melt compositions encompassing the geochemical range of the region, with Th and the REE in filled symbols and the conservative elements (CEs; see text) in open symbols. Bottom panels isolate the CEs, with bold and dashed lines showing model curves for the CE patterns, varying $F$ and $C^o_{Ti}$ as illustrated in Figure 6. The shaded fields around these model curves illustrate the errors on the model (see Table 1), constrained by determining the range of model pattern shapes permissible by any pair of CEs (including 10% errors in the concentration of each element; see text). Within a given basin, segments with similar mantle characteristics are grouped together. (a, b) Mariana trough. (c, d) Manus basin, ER segment. (e, f) Manus basin, MSC, ETZ, and SR segments. (g, h) Lau basin, MTJ and ILSC segments. (i, j) Lau basin, CLSC segment. (k, l) Lau basin, ELSC and VFR segments, with additional curve (solid shaded line) illustrating the misfit of a variable $C^o_{Ti}$-constant $F$ model. (m, n) Sumisu rift. (o, p) Woodlark basin, NE segment. (q, r) Woodlark basin, east segment. (s, t) East Scotia ridge, E2–E4 segments. (u, v) East Scotia ridge, E5–E6 segments. (w, x) East Scotia ridge, E7–E8 segments. See text for data sources.

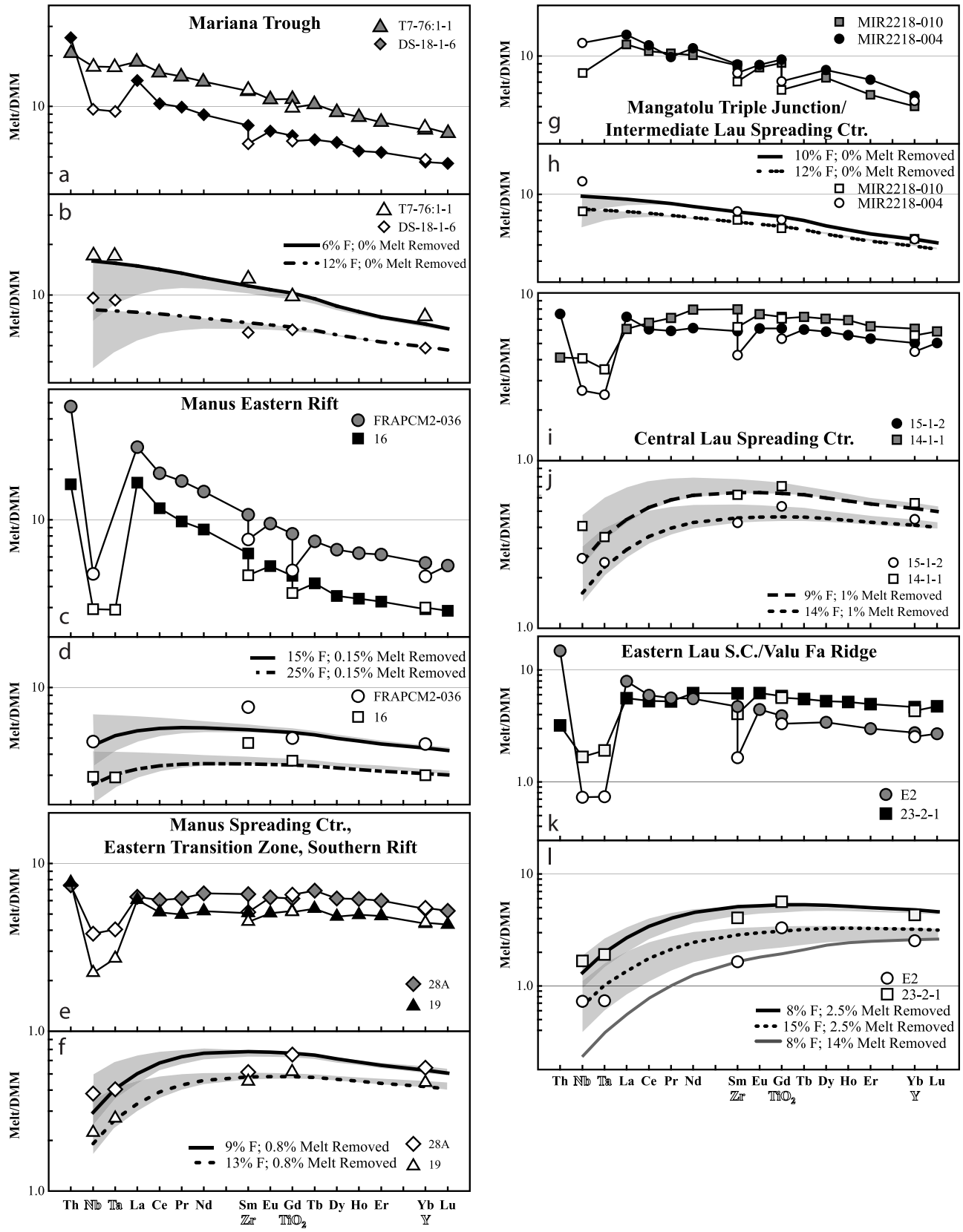
Mariana Trough
T7-76:1-1
DS-18-1-6
a
b
6% F; 0% Melt Removed
12% F; 0% Melt Removed
Manus Eastern Rift
FRAPCM2-036
16
c
d
15% F; 0.15% Melt Removed
25% F; 0.15% Melt Removed
Manus Spreading Ctr.,
Eastern Transition Zone, Southern Rift
28A
19
e
f
9% F; 0.8% Melt Removed
13% F; 0.8% Melt Removed
MIR2218-010
MIR2218-004
g
Mangatolu Triple Junction/
Intermediate Lau Spreading Ctr.
h
10% F; 0% Melt Removed
12% F; 0% Melt Removed
i
Central Lau Spreading Ctr.
15-1-2
14-1-1
j
9% F; 1% Melt Removed
14% F; 1% Melt Removed
Eastern Lau S.C./Valu Fa Ridge
E2
23-2-1
k
l
8% F; 2.5% Melt Removed
15% F; 2.5% Melt Removed
8% F; 14% Melt Removed
Melt/DMM
Th Nb Ta La Ce Pr Nd Sm Eu Gd Tb Dy Ho Er Yb Lu
Zr TiO2 Y

**Figure 7**

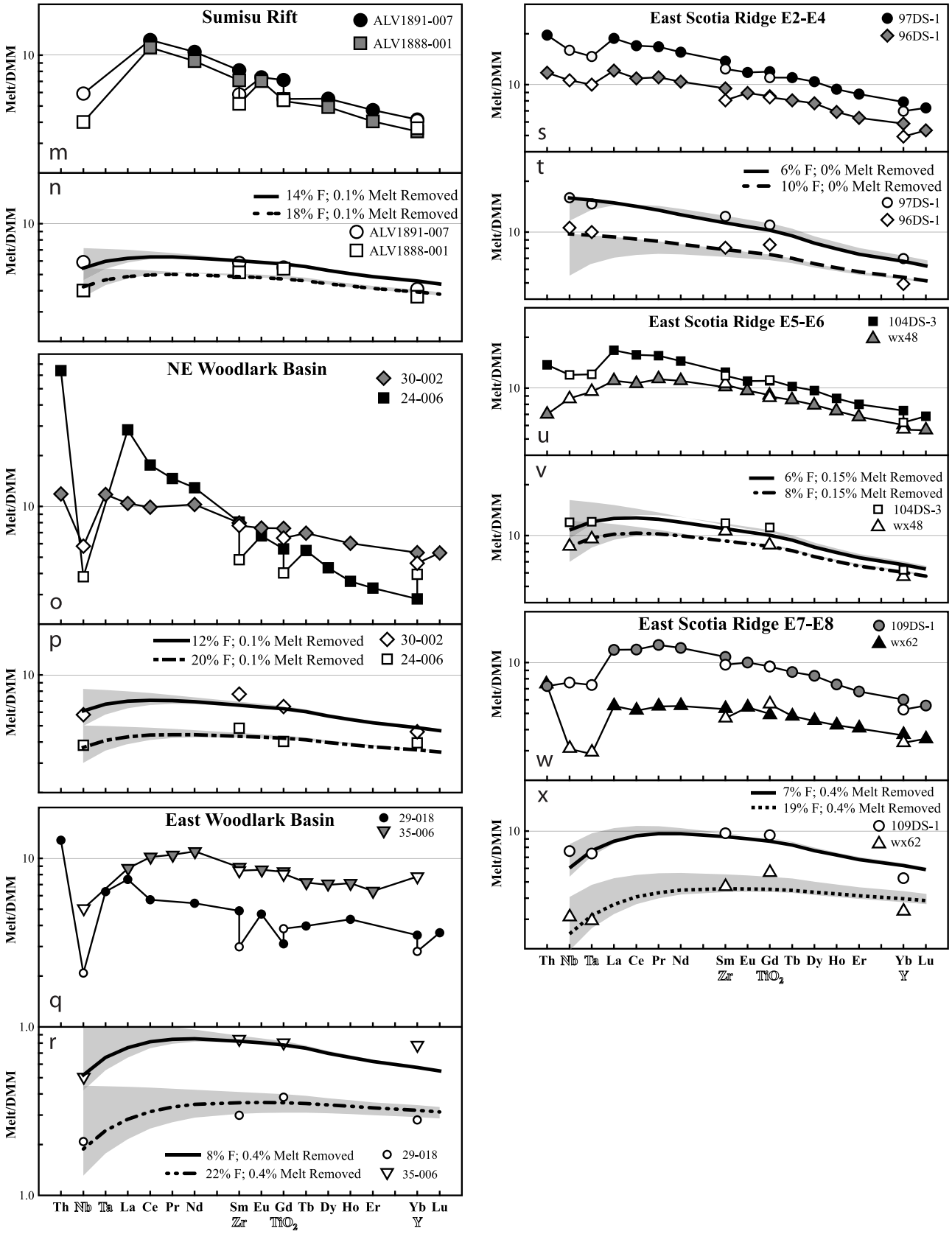


**Figure 7.** (continued)

patible elements (e.g., Nb and Ta), which may change in source concentration by a factor of 10 with as little as 2.5% melt removed, whereas $TiO_2$ would vary by only a factor of 1.5, using the batch melting model. Removing melt using a fractional melting model would lead to even smaller changes in $TiO_2$ relative to the more incompatible elements, and we thus used the batch removal model because it allows for greater variation of $TiO_2$ in the mantle source. The concentration of Nb or Ta, relative to $TiO_2$ (and other elements), therefore provides a constraint on the amount of depletion necessary in the mantle source of each region. This constraint is a minimum in the sense that Nb and Ta could theoretically be added from the slab, causing the mantle to appear less depleted than it actually is. These constraints are then used to estimate the mantle source composition and $C^o_{Ti}$ for most back-arc spreading segments (Table 1, Figure 7), and we apply a constant source composition to each segment. We unfortunately cannot, in many cases, perform this analysis with the exact samples used to model $F$ and $H_2O_o$ because most of these glasses do not have the necessary trace element data. In such cases, trace element data from whole rock samples in the same local area were used to establish regional source characteristics beneath each spreading segment [*Hochstaedter et al.*, 1990b; *Nohara et al.*, 1994; *Pearce et al.*, 1995; *Dril et al.*, 1997; *Fretzdorff et al.*, 2002; *Sinton et al.*, 2003].

[19] Figure 7 illustrates back-arc regions where the mantle sources were successfully modeled relative to DMM. The conservative elements (CEs) Nb, Ta, Zr, Ti, and Y reflect mantle source characteristics, whereas rare earth elements and Th indicate the extent of geochemical enrichment from the slab. As a general rule, lavas with lower absolute concentrations of CEs (i.e., higher $F$) show greater absolute abundances in slab-derived elements than low-$F$ lavas from the same regions, suggesting a link between $F$ and the extent of slab-derived input at back-arc basins (such that larger extents of melting are associated with greater slab input of the non-CEs). The mantle depletion model developed here makes a fair approximation of the CE patterns and thus the mantle source characteristics of basins and intrabasin segments tapping variably depleted mantle. In fact, most regions require little to no prior melt removal ($f <$ 0.2%) to explain the CE patterns (e.g., Mariana trough, Sumisu rift, MTJ, ILSC, Manus ER, ESR E2–E6, Woodlark basin NE (Table 1)). The CE patterns are also generally parallel within a given basin spreading segment ($F$ variation) rather than of variable shape (source variation), which supports the assertion that $F$ is the dominant variable controlling CE variation on local scales. A few regions require more depleted mantle (~1–2.5% $f$; e.g., CLSC, ELSC-VFR, Manus MSC-ETZ (Table 1)), which relates to low Nb concentrations (<1 ppm).

[20] We acknowledge that the model curves are not perfect fits to the CE patterns in Figure 7, likely due to variable data quality (particularly for Nb and Ta) and possible additions from the slab in some cases. Conservative trace element variations could, alternatively, arise dominantly or exclusively from variations in mantle source composition. We evaluated this possibility by holding $F$ constant and attempting to fit the CE patterns of lavas only through changing mantle depletion. This model falls short in two ways. First, the extent of prior melt removal necessary to explain variations in the less incompatible elements Zr and Y removes too much Nb and Ta to match the shape of the full CE pattern in multiple samples from a given region (e.g., Figure 7l). Niobium and tantalum could, however, be added from the slab, which would elevate their concentrations above the ambient mantle and explain why the full CE pattern is poorly modeled. Second, the extents of prior melt removal ($f$) necessary to broadly reproduce the

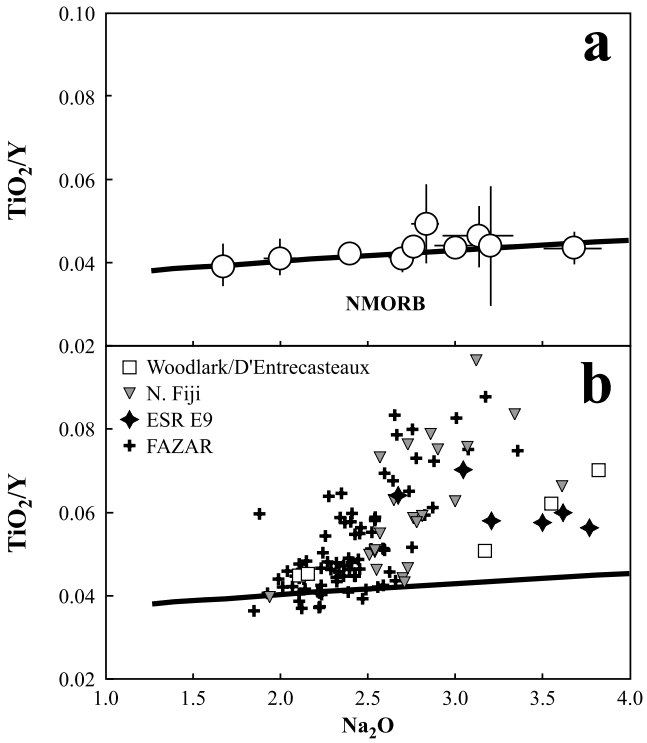


**Figure 8.** $TiO_2$/Y versus $Na_2O$, demonstrating the model used to constrain mantle source characteristics for segments with enriched mantle sources (more trace element enriched than the DMM of *Salters and Stracke* [2004]). $TiO_2$ and Y have similar mantle/melt $D$s for N-MORB, whereas absolute concentrations of incompatible elements like $Na_2O$, which are relatively invariant in the mantle source, vary systematically as a function of $F$. (a) $TiO_2$/Y versus $Na_2O$ in MORB, with a batch melting model curve (bold line) approximating the MORB trend, showing the relative invariance of the $TiO_2$/Y ratio with extent of melting at mid-ocean ridges. Regional MORB averages (samples with 7.5–8.5 wt % MgO) are from the following regions: the Kolbeinsey ridge [*Devey et al.*, 1994], the Australian-Antarctic discordance [*Klein et al.*, 1991], the Indian Ocean triple junction [*Price et al.*, 1986], the Tamayo region [*Bender et al.*, 1984], the Pacific seamounts [*Niu and Batiza*, 1997], the Cayman rise and the Reykjanes ridge (www.petdb.org), and the Mid-Atlantic Ridge between the Kane and Hayes fracture zones (www.petdb.org). Error bars are one standard deviation of the regional average. (b) $TiO_2$/Y versus $Na_2O$ in ridge and back-arc regions with enriched mantle (Table 1) showing high $TiO_2$/Y, attributed here to source enrichment. The points shown are individual glass samples. The bold line is the MORB batch melting model curve from Figure 8a.

geochemical range recorded, for example, along the Lau basin (Figure 7l) would correlate with variations in $H_2O$ concentration along the length of the basin, and indeed in global basins. The Lau basin mantle composition clearly varies along strike regardless of how we model it, but there is no strong argument for why large variations of $H_2O$ concentrations in the source regions of arcs and back arcs should correlate globally with the extent of prior mantle depletion [*Eiler et al.*, 2000]. Water concentrations more sensibly correlate with additions of slab-derived components and with $F$. We therefore elect to constrain variations in the water-poor, MORB-like component of the mantle beneath back-arc basins using the approach described above whereby this component is assumed to have been derived from DMM by variable amounts of prior batch melt extraction, and where the amount of this prior melt extraction is constrained using a fit to the HFSE that assumes they are truly conservative (i.e., uninfluenced by the addition of water-rich, slab-derived components). To the degree that these conservative elements might have been influenced by addition from the slab, the absolute magnitude of their variations in the MORB-like component in the sources of back-arc magmas may require modification, and the source constraints we present (Table 1) would represent the minimum amount of depletion (and therefore the maximum $C^o_{Ti}$) necessary to explain the geochemistry of these back-arc basins.

### 2.5. Modeling Enriched Mantle Source Compositions

[21] The melt removal–based source model also only succeeds in regions where the mantle is similar to, or more depleted than, the initial DMM composition. In regions where the mantle is more trace element–enriched than DMM, the trace element patterns have steeper negative slopes than unmodified DMM and cannot be explained by prior melt removal from this MORB-like source. In such cases we employed another approach to approximating the $H_2O$-poor mantle sources. In the case of the Galápagos spreading center, we adopted the source constraints of *Cushman et al.* [2004], but in other regions where enriched mantle source characteristics have not been so rigorously evaluated, we applied a simple model based on $TiO_2/Y$ systematics. The ratio of $TiO_2$ to Y varies little during mantle melting at mid-ocean ridges ($TiO_2/Y$ = 0.04–0.05 for regionally averaged MORB (Figure 8)) because these elements have similar mantle/melt $D$s. On the other hand, regions near hot spots or having previously recognized, isotopically enriched mantle have high $TiO_2/Y$ ratios (e.g., FAZAR, N. Fiji basin (Figure 8) [*Eissen et al.*, 1994; *Asimow et al.*, 2004]). Some of the high ratios could arise from a higher $D_Y$ in these sources (which could contain garnet), but we elect to treat $TiO_2/Y$ ratios in excess of mean MORB entirely as $TiO_2$ enrichment of the $H_2O$-poor mantle source, in order to provide a maximum constraint on $C^o_{Ti}$; that is,

$$C^o_{Ti} = \left[\frac{(TiO_2/Y)_{sample}}{(TiO_2/Y)_{MORB}}\right] \times C^{DMM}_{Ti}, \quad (11)$$

where $(TiO_2/Y)_{sample}$ is the $TiO_2/Y$ ratio of the glass, $(TiO_2/Y)_{MORB}$ is 0.04, and $C^{DMM}_{Ti}$ is 0.133 (Table 2). This likely overestimates $C^o_{Ti}$ and leads to maximum values for $F$ and $H_2O_o$. We thus present the results below using a range of $C^o_{Ti}$ values, but in all cases comparing results using the constant source model (DMM [*Salters and Stracke*, 2004]) to maximum $C^o_{Ti}$ constraints from $TiO_2/Y$ in enriched regions and CE constraints for depleted regions (Table 1).

### 2.6. Uncertainties and Errors

[22] The effects of uncertainties in measurements and model assumptions on the final calculations of $F$ and $H_2O_o$ require careful consideration. We first addressed the confidence level of each source of uncertainty. For analytical measurements ($TiO_2$ and $H_2O$), we used the standard deviation of replicate measurements on any given sample to reflect the uncertainty in the data (±5% for $TiO_2$, ±10% for $H_2O$). For $C^l_{Ti}$, both the correction for crystal fractionation and the possibility of slab-derived $TiO_2$ in the melt contribute to errors in this value, and we used an uncertainty of ±20%. Minimum errors in the mantle source composition ($C^o_{Ti}$) arise from analytical uncertainties in the measurement of the CEs used to constrain the source characteristics. Uncertainties on $C^o_{Ti}$ were thus constrained by allowing 10% variation in all of the CEs in the melt removal model for each region and by constraining the full range of $f$ values (as shown by pattern shapes in Figure 7) permissible by any pair of CEs within this 10% concentration variation (see Table 1). On average, this analysis results in $\leq$10% error in $C^o_{Ti}$. We explored the effect of a ±50% variation in $D_{Ti}$ (0.02–0.06), which encompasses the range over which the instantaneous value of $D_{Ti}$ may vary along a polybaric path (see section 2.3 [*Langmuir et al.*, 1992]). The $D_{H_2O}$ (0.012) used here originates from S&N94 and is consistent with the $D_{Ce}$ used here (Table 2), but recent experiments suggest lower values for both $D_{H_2O}$ and $D_{Ce}$ during batch melting of spinel lherzolite (0.007–0.009 [*Aubaud et al.*, 2004; *Hauri et al.*, 2006]. Studies of MORB and OIB data also suggest a lower value for $D_{H_2O}$, closer to $D_{La}$ (0.01 [*Dixon et al.*, 2002]), and we thus also evaluated the effect of lowering $D_{H_2O}$ in our error analysis but use $D_{H_2O}$ = 0.012 for the final calculations to remain consistent with S&N94. An additional test of the modeling outcome, using $Na_2O$ instead of $TiO_2$ as a proxy for $F$, is provided in the auxiliary material[1]. Using this alternate proxy for $F$ yields results similar to those for $TiO_2$. Our results are thus not dependent on the use of $TiO_2$ as a proxy for $F$, nor on factors specific to $TiO_2$ (e.g., the presence of rutile, ilmenite, and Ti-clinohumite in the mantle).

[23] We used a Monte Carlo error analysis, which allows each parameter to vary simultaneously within its assigned uncertainty during the calculation of $F$ and $H_2O_o$, to evaluate the effects of these uncertainties on the model trends. This technique produces error ellipses around the modeled points in $H_2O_o$ versus $F$, which represent the outcome of 90% of the trial calculations (Figure 9a). Elongation of the ellipses relative to the origin is largely a product of the uncertainties in $C^o_{Ti}$ and $D_{Ti}$, but also serves to emphasize that errors on this diagram are highly correlated. $F$ is used to calculate $H_2O_o$, and any error contributing to the determination of $F$ therefore propagates into error in

[1] Auxiliary materials are available in the HTML. doi:10.1029/2005JB003732.

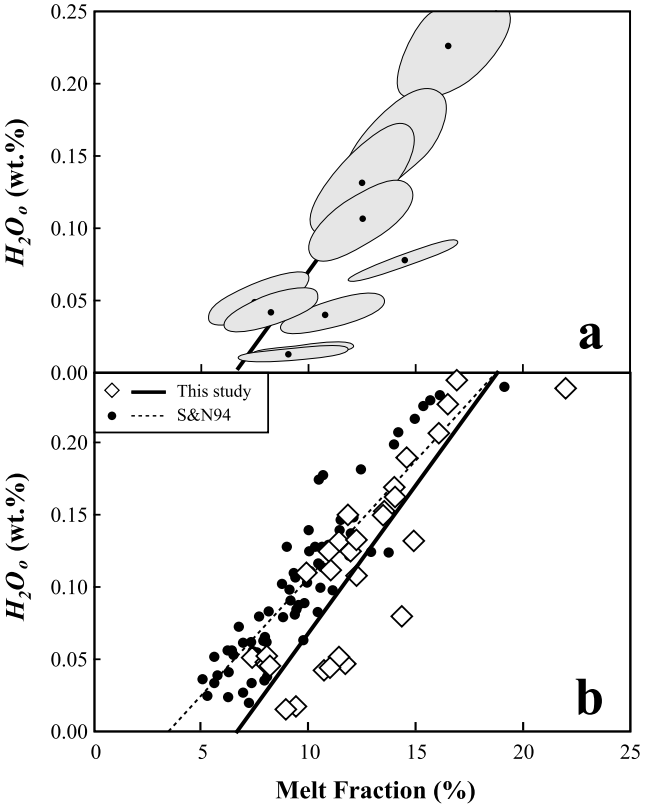


**Figure 9.** $H_2O_o$ ($H_2O$ concentration of the mantle source) versus $F$ (mantle melt fraction) showing (a) error ellipses for 10 example points in the Mariana trough (MT). The bold line is a linear regression through the full MT data set, as shown in Figure 10a. The equation of the line is $y = 2.082x - 0.142$ ($r^2 = 0.798$), errors on the slope are ±10%, and errors on the intercept are ±30%. (b) Comparison between results of S&N94 and this study. The black circles and short-dashed line are the results and linear best fit from S&N94 ($y = 1.628x - 0.055$; $r^2 = 0.840$). The open diamonds are the results from this study, utilizing a larger initial glass data set than S&N94, and the solid line is the best fit line to these points ($y = 2.082x - 0.142$; $r^2 = 0.798$). This study filtered the data differently than did S&N94, which is why this study plots fewer points.

$H_2O_o$. This analysis results in up to 30% uncertainty in the $F$-intercept (melt fraction at zero $H_2O_o$) of a regressed line but relatively little variation in the slope (~10%), which indicates that the slopes of the model trends are more robust than the intercepts.

[24] Both the S&N94 method and the procedure outlined here result in similar trends despite employing different geochemical constraints and data sets for determining $F$ and $H_2O_o$ in the Mariana trough. Figure 9b compares the results from S&N94 with the results from this study. For the two best-fit lines shown in Figure 9b (one regressed through the S&N94 points and the other through the points from this work), the absolute difference in $F$-intercept is large (3.4 versus 7.0%), owing in part to the extra steps taken here to correct for crystal fractionation, which result in lower $TiO_2$ in the modeled melt compositions. The slopes of the two trends, however, differ by only 28% (1.63 versus 2.08). This difference in slope translates into relatively small differences in $H_2O_o$ at a given $F$ (e.g., 0.07 versus 0.10 wt % $H_2O_o$ at $F$ = 10%), and is probably within the analytical uncertainty in the $H_2O$ measurement. We regard this comparison as a successful reproduction of the original S&N94 trend, using the $TiO_2$ proxy for $F$.

### 2.7. Mantle Temperature, Axial Depth, Crustal Thickness, and Melt Production

[25] Mantle potential temperature ($T_p$) is a primary factor in melt production at mid-ocean ridges, and it likely strongly influences melt generation beneath back-arc basins as well. At ridges, mantle $T_p$ controls the depth/pressure at which melting initiates ($P_o$) and thus the overall extent of melting ($F$), which relates to the length of the melting column [*Klein and Langmuir*, 1987; *McKenzie and Bickle*, 1988]. The FeO concentration of a melt is sensitive to $P_o$, whereas the concentrations of incompatible elements such as $Na_2O$ or $TiO_2$ vary inversely with $F$ [*Klein and Langmuir*, 1987; *Kinzler and Grove*, 1992]. In Figure 2, the correlation of global MORBs in $Na_{(Fo90)}$ versus $Fe_{(Fo90)}$ (i.e., $Na_2O$ and FeO concentrations corrected for crystal fractionation to equilibrium with $Fo_{90}$; see section 2.1) is consistent with variations in $T_p$ and $P_o$ [*Langmuir et al.*, 1992; *Kinzler*, 1997; *Asimow et al.*, 2001]. We used the pooled, accumulated fractional melting model of *Langmuir et al.* [1992] to calculate $T_p$ from dry, MORB-like back-arc basin melts ($H_2O \leq 0.5$ wt % (Figure 2, Tables 3 and 4)) using $Na_{(Fo90)}$ and $Fe_{(Fo90)}$ parameterized as follows:

$$T_p(\mathrm{Fe}) = \left[3.4381 \times \left(\mathrm{Fe}_{(\mathrm{Fo90})}\right)^2\right] + \left[4.154 \times \left(\mathrm{Fe}_{(\mathrm{Fo90})}\right)\right] + 1088.6 \quad (12)$$

$$T_p(\mathrm{Na}) = \left[41.164 \times \left(\mathrm{Na}_{(\mathrm{Fo90})}\right)^2\right] - \left[336.78 \times \left(\mathrm{Na}_{(\mathrm{Fo90})}\right)\right] + 1956.1. \quad (13)$$

Values of $T_p$ were calculated for each mid-ocean ridge and back-arc basin by averaging $T_p$(Fe) and $T_p$(Na) for each sample, then averaging $T_p$(sample) for all samples in each basin (Table 4). In the few cases where the standard deviation between the two $T_p$ calculations from a single glass composition was >50°C, then only $T_p$(Na) was used in the regional average because the correction of Fe concentrations in high-Fe glasses to $Fo_{90}$ has greater error than the Na correction.

[26] Axial depth and crustal thickness at mid-ocean ridges are also linked to total melt production, reflecting the integrated effects of mantle temperature, wet melting, and melt removal. High mantle temperature and large extents of melting combine to generate thick oceanic crust that, due to isostasy, lies at shallower water depths (i.e., lower axial depth) than regions with thinner crust. Axial depth and crustal thickness relate quantitatively to the extent of melting as reflected, for example, by the correlation of depth with melt fraction proxies (e.g., $Na_{8.0}$ [*Klein and Langmuir*, 1987]; see Figure 1). In order to explore the extent to which the chemical and physical relationships observed at mid-ocean ridges extend to back-arc basins, we determined mean axial depths at back-arc basins either from

**Table 3.** Geochemical Variables at Back-Arc Basins

| | | Dry Samples Only ($H_2O$ < 0.5 wt %) | | | | | | All Samples | | | | | |
|---|---|---|---|---|---|---|---|---|---|---|---|---|---|
| Basin | Segment | $CaO/Al_2O_3$ | 1σ | $Fe_{(Fo90)}$ | 1σ | $Na_{(Fo90)}$ | 1σ | $CaO/Al_2O_3$ | 1σ | $Fe_{(Fo90)}$ | 1σ | $Na_{(Fo90)}$ | 1σ |
| | | | | | | *Small-Scale Averages* | | | | | | | |
| East Scotia ridge | E2–E4 | 0.69 | 0.02 | 7.48 | 0.46 | 2.66 | 0.13 | 0.68 | 0.01 | 6.62 | 0.25 | 2.62 | 0.07 |
| | E5–E8 | 0.73 | 0.01 | 8.18 | 0.11 | 2.69 | 0.07 | 0.73 | 0.01 | 8.07 | 0.15 | 2.70 | 0.07 |
| | E9 | 0.71 | 0.02 | 7.03 | 0.08 | 3.06 | 0.04 | 0.71 | 0.02 | 6.49 | 0.41 | 2.85 | 0.20 |
| Lau basin | MTJ | 0.76 | 0.02 | 9.08 | 0.18 | 2.20 | 0.04 | 0.79 | 0.02 | 8.24 | 0.27 | 2.17 | 0.07 |
| | CLSC | 0.82 | 0.02 | 9.51 | 0.25 | 1.92 | 0.03 | 0.82 | 0.02 | 9.51 | 0.25 | 1.92 | 0.03 |
| | ILSC | 0.76 | 0.03 | 8.22 | 0.47 | 1.84 | 0.18 | 0.76 | 0.03 | 8.22 | 0.47 | 1.84 | 0.18 |
| | ELSC | 0.79 | 0.01 | 8.76 | 0.40 | 1.55 | 0.04 | 0.80 | 0.01 | 8.73 | 0.23 | 1.57 | 0.07 |
| | VFR | | | | | | | 0.86 | 0.01 | 10.34 | 0.41 | 1.12 | 0.06 |
| Manus basin | ER | | | | | | | 0.76 | 0.09 | 8.35 | 0.00 | 1.28 | 0.00 |
| | MSC-ETZ | 0.85 | 0.00 | 10.46 | 0.08 | 1.68 | 0.04 | 0.83 | 0.02 | 9.54 | 0.41 | 1.63 | 0.04 |
| Mariana trough | 15°–17°N | 0.69 | 0.07 | 8.04 | 0.14 | 2.68 | 0.12 | 0.68 | 0.01 | 7.01 | 0.30 | 2.52 | 0.08 |
| | 17°–19°N | 0.69 | 0.05 | 7.22 | 1.08 | 2.79 | 0.07 | 0.66 | 0.01 | 6.45 | 0.23 | 2.54 | 0.06 |
| | 19°–21°N | | | | | | | 0.67 | 0.01 | 6.70 | 0.49 | 2.39 | 0.15 |
| North Fiji basin | N160° | 0.73 | 0.00 | 8.60 | 0.00 | 2.30 | 0.00 | 0.67 | 0.03 | 6.11 | 0.57 | 2.53 | 0.14 |
| | TJ | 0.73 | 0.04 | 8.59 | 0.37 | 2.17 | 0.02 | 0.73 | 0.04 | 8.59 | 0.37 | 2.17 | 0.02 |
| Woodlark basin | D'Entrecasteaux | | | | | | | 0.66 | 0.00 | 6.24 | 0.06 | 2.73 | 0.02 |
| | center | 0.76 | 0.00 | 8.71 | 0.06 | 2.32 | 0.03 | 0.76 | 0.00 | 8.71 | 0.06 | 2.32 | 0.03 |
| | east | 0.71 | 0.02 | 8.46 | 0.14 | 2.77 | 0.04 | 0.67 | 0.03 | 7.74 | 0.73 | 2.58 | 0.18 |
| | | | | | | *Basin-Scale Averages* | | | | | | | |
| East Scotia ridge | whole | 0.72 | 0.01 | | | | | 0.70 | 0.01 | | | | |
| Lau basin | north | 0.79 | 0.01 | 8.98 | 0.17 | 2.04 | 0.04 | 0.80 | 0.01 | 8.73 | 0.21 | 2.04 | 0.05 |
| | south | 0.79 | 0.01 | 8.76 | 0.40 | 1.55 | 0.04 | 0.85 | 0.01 | 9.91 | 0.34 | 1.24 | 0.06 |
| Manus basin | whole | 0.85 | 0.00 | 10.46 | 0.08 | 1.68 | 0.04 | 0.81 | 0.03 | 9.32 | 0.38 | 1.60 | 0.04 |
| Mariana trough | whole | 0.69 | 0.04 | 7.66 | 0.36 | 2.72 | 0.09 | 0.67 | 0.01 | 6.69 | 0.18 | 2.50 | 0.05 |
| Sumisu rift | whole | | | | | | | 0.70 | 0.03 | 9.27 | 0.59 | 2.04 | 0.02 |
| North Fiji basin | whole | 0.74 | 0.01 | 8.59 | 0.33 | 2.19 | 0.03 | 0.70 | 0.01 | 7.97 | 0.49 | 2.28 | 0.07 |
| Woodlark basin | whole | 0.74 | 0.01 | 8.61 | 0.07 | 2.49 | 0.07 | 0.74 | 0.03 | 7.93 | 0.33 | 2.49 | 0.07 |

the axial profiles of *Taylor and Martinez* [2003] for the four basins they examined or from averaging the sample collection depths for the other basins we have examined in our study (see Table 4). We also estimated crustal thickness (see Table 4) from seismic profiles of the few basins where detailed geophysical data exist [*Bibee et al.*, 1980; *LaTraille and Hussong*, 1980; *Ambos and Hussong*, 1982; *Turner et al.*, 1999; *Crawford et al.*, 2003; *Martinez and Taylor*, 2003].

### 2.8. Summary of Methods

[27] We have described in detail the several steps in our treatment of glass compositions from back-arc basins, and we summarize them here. The compiled basalt data were first screened to exclude fractionated compositions (MgO < 7.0 wt %) and degassed samples (pure $H_2O$ saturation pressure <30 bars from eruption pressure). All remaining glasses were then corrected for the effects of crystal fractionation, adjusting the melt compositions to olivine-enriched compositions that would be in equilibrium with $Fo_{90}$. The extent of melting of a peridotitic mantle source ($F$) required to produce each corrected back-arc basin glass composition was calculated based on its $TiO_2$ content relative to its mantle source using the batch melting equation and a constant $D_{Ti}$. The concentration of $H_2O$ in the mantle source of each sample was then calculated using this value of $F$ and a constant $D_{H_2O}$. Note that the calculations of $F$ require knowledge of the $TiO_2$ content of the mantle source ($C^o_{Ti}$) of each sample prior to melting. We have shown that $TiO_2$ contents of most back-arc mantle sources (prior to addition of slab-derived components) can be modeled using the DMM composition of *Salters and Stracke* [2004], but in some cases the deviation from this end-member appears to be significant. For mantle lower in $TiO_2$ than DMM, we adjusted $C^o_{Ti}$ for each spreading segment using conservative elements (Nb, Ta, Zr, $TiO_2$, Y), assuming that the concentrations of these elements deviate from DMM due to a previous episode of melt extraction (assumed to be batch melting). For sources enriched in trace elements relative to DMM (again, prior to addition of slab-derived components), we modeled $C^o_{Ti}$ based on their $TiO_2$/Y ratios. The total variation in $C^o_{Ti}$ from region to region is a little more than a factor of 2. A Monte Carlo error analysis reveals uncertainties on the linear regression through the modeled Mariana trough data of ~30% on the $F$-intercept and ~10% on the slope of the line, and the trend of $F$ and $H_2O_o$ determined using this procedure is similar to that first shown in this region by S&N94 (see Figure 9b).

## 3. Results

[28] Here we present a summary of the modeling outcome for back-arc basins and mid-ocean ridges. Detailed discussions of the results for each specific region are presented in the auxiliary material. The correlation of $TiO_{2(Fo90)}$ and $H_2O_{(Fo90)}$ in the fractionation-corrected glass data illustrate the first-order observations suggesting a relationship between $H_2O$ and mantle melting in back-arc basin settings. Most of the back-arc basin data show dominant trends of decreasing $TiO_{2(Fo90)}$ with increasing $H_2O_{(Fo90)}$ (Figure 4). Because $TiO_2$ is incompatible during mantle melting, and we assume $TiO_2$ originates only from the mantle, we expect that its concentration in the melt will be progressively diluted as the melt fraction ($F$) increases. The relationships shown in Figures 4a, 4c, and 4d thus suggest

**Table 4.** Physical Variables at Back-Arc Basins

| Basin | Segment | Arc Distance, km | 1σ | Trench Distance, km | 1σ | Axial Depth, m | 1σ | $C_T$, km | Mean $F$ | 1σ | Mean $H_2O_o$, wt % | 1σ | $T_p$, °C | ± | $dF/dH_2O_o$ | ± | $F$-Intercept, % | $r^2$ |
|---|---|---|---|---|---|---|---|---|---|---|---|---|---|---|---|---|---|---|
| *Small-Scale Averages* | | | | | | | | | | | | | | | | | | |
| East Scotia ridge | E2–E4 | 200 | 5 | 361 | 4 | −3275 | 73 | | 0.10 | 0.00 | 0.08 | 0.01 | 1343 | 12 | | | | |
| | E5–E8 | 217 | 7 | 370 | 6 | −3748 | 53 | | 0.07 | 0.00 | 0.02 | 0.00 | 1355 | 7 | | | | |
| | E9 | 117 | 3 | 291 | 10 | −2690 | 124 | | 0.21 | 0.11 | 0.21 | 0.04 | 1299 | 0 | | | | |
| Lau basin | MTJ | 158 | 24 | 293 | 18 | −2152 | 58 | | 0.12 | 0.01 | 0.07 | 0.01 | 1410 | 8 | | | | |
| | CLSC | 268 | 1 | 400 | 0 | −2296 | 11 | 7–8 | 0.11 | 0.00 | 0.04 | 0.00 | 1461 | 6 | | | | |
| | ILSC | 209 | 8 | 346 | 4 | −2950 | 100 | | 0.15 | 0.03 | 0.06 | 0.02 | | | | | | |
| | ELSC | 162 | 8 | 313 | 2 | −2541 | 15 | 5.5–6.5 | 0.09 | 0.00 | 0.04 | 0.01 | | | | | | |
| | VFR | 127 | 1 | 260 | 1 | −1957 | 12 | 8 | 0.14 | 0.01 | 0.22 | 0.04 | | | | | | |
| Manus basin | ER | 174 | 3 | 280 | 18 | −1843 | 75 | | 0.38 | | 0.38 | | | | | | | |
| | MSC-ETZ | 274 | 8 | 402 | 5 | −2329 | 34 | | 0.18 | 0.02 | 0.10 | 0.03 | | | | | | |
| Mariana trough | 15°–17°N | 98 | 2 | 323 | 2 | −3997 | 24 | | 0.12 | 0.01 | 0.11 | 0.02 | 1355 | 10 | | | | |
| | 17°–19°N | 107 | 2 | 317 | 1 | −4287 | 28 | | 0.13 | 0.01 | 0.13 | 0.02 | 1338 | 8 | | | | |
| | 19°–21°N | 111 | 6 | 331 | 7 | −4347 | 25 | | 0.12 | 0.01 | 0.12 | 0.03 | 1415 | 16 | | | | |
| Woodlark basin | D'Entrecasteaux | | | | | −2669 | 0 | | 0.15 | 0.02 | 0.10 | 0.01 | | | | | | |
| | center | | | | | −3819 | 85 | | 0.06 | 0.00 | 0.01 | 0.00 | 1391 | 3 | | | | |
| | east | | | | | −3238 | 174 | | 0.12 | 0.04 | 0.08 | 0.07 | 1355 | 3 | | | | |
| North Fiji basin | N160° | 626 | 30 | 926 | 73 | −3554 | 52 | | 0.12 | 0.03 | 0.07 | 0.00 | 1389 | 14 | | | | |
| | TJ | 621 | 15 | 751 | 20 | −2658 | 260 | | 0.14 | 0.01 | 0.03 | 0.00 | 1409 | 11 | | | | |
| *Basin-Scale Averages* | | | | | | | | | | | | | | | | | | |
| East Scotia ridge | whole | 197 | 6 | 356 | 5 | −3363 | 59 | | 0.09 | 0.01 | 0.05 | 0.01 | 1348 | 7 | 0.32 | 0.04 | 5.1 | 0.848 |
| Lau basin | north | 207 | 15 | 342 | 13 | −2309 | 9 | | 0.12 | 0.01 | 0.05 | 0.01 | 1440 | 7 | 0.66 | 0.07 | 7.9 | 0.710 |
| | south | 136 | 4 | 273 | 6 | −2273 | 19 | | 0.14 | 0.01 | 0.22 | 0.04 | | | 0.29 | 0.02 | 7.7 | 0.910 |
| Manus basin | whole | 249 | 17 | 372 | 21 | −2153 | 12 | | 0.12 | 0.04 | 0.19 | 0.03 | 1505 | 9 | 0.77 | 0.05 | 10.1 | 0.951 |
| Mariana trough | whole | 105 | 2 | 321 | 2 | −4222 | 16 | 4–7 | 0.15 | 0.03 | 0.19 | 0.05 | 1354 | 10 | 0.48 | 0.04 | 6.9 | 0.798 |
| Woodlark basin | whole | | | | | −3366 | 127 | | 0.10 | 0.02 | 0.05 | 0.03 | 1377 | 5 | 0.67 | 0.05 | 6.7 | 0.923 |
| Sumisu rift | whole | 16 | 2 | 229 | 3 | −1911 | 123 | | 0.18 | 0.01 | 0.16 | 0.02 | | | | | | |
| North Fiji basin | whole | 623 | 13 | 817 | 42 | −2994 | 227 | | 0.13 | 0.01 | 0.05 | 0.01 | 1406 | 9 | | | | |

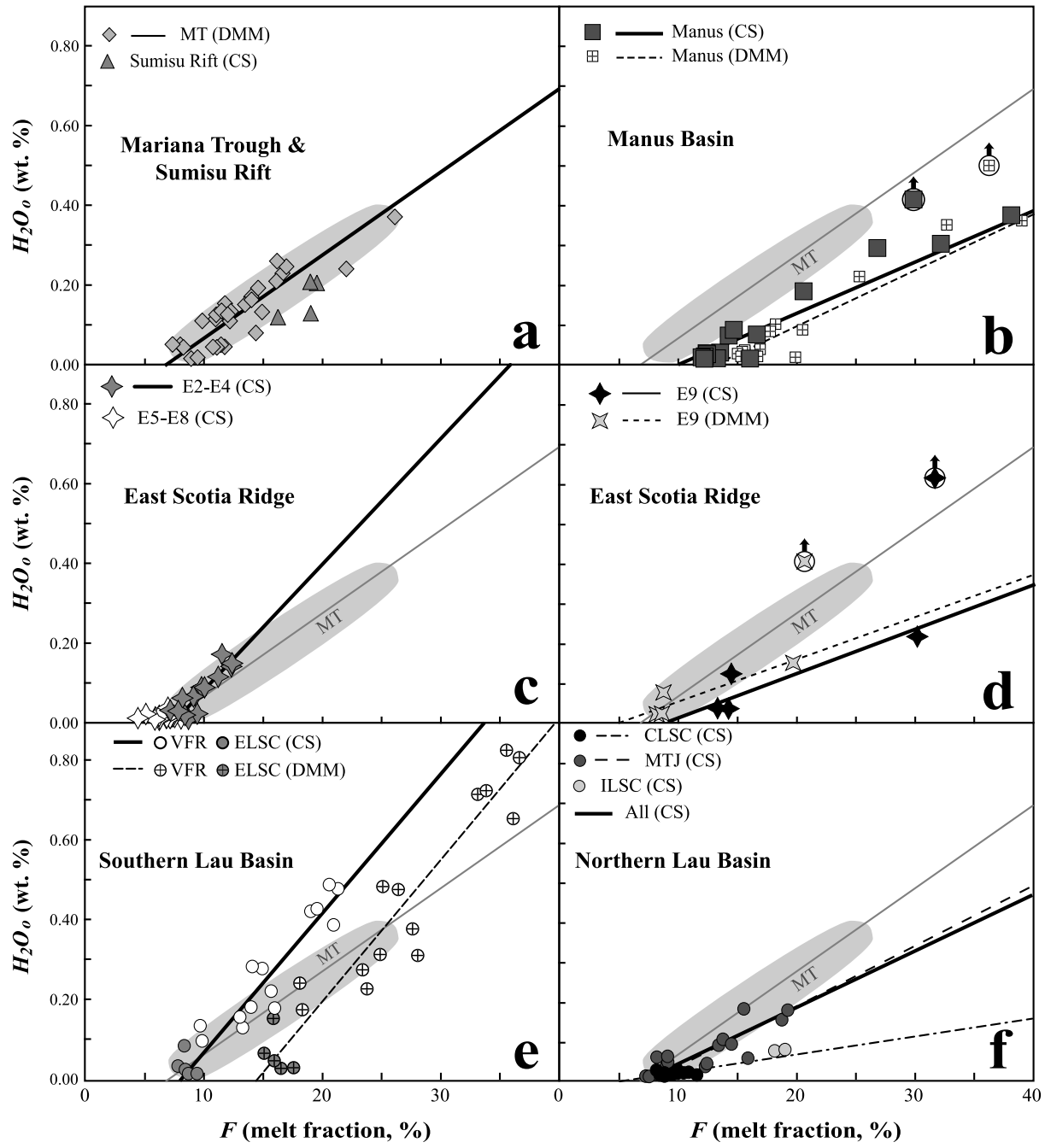


**Figure 10.** $H_2O_o$ versus $F$ at back-arc basins closely associated with subduction. The light shaded field and the dark shaded line are the range of Mariana trough model points and the linear regression from Figure 9b. The results using a constant MORB mantle source ($C^o_{Ti} = 0.133$) are labeled DMM, and results using variable mantle source constraints modeled in this work are labeled CS (corrected source; $C^o_{Ti}$ given in Table 1). In many cases, the DMM and CS results were too similar to distinguish, and in these cases, only CS results are shown. (a) Mariana trough (CS, $y = 2.082x - 0.142$; $r^2 = 0.798$) and the Sumisu rift (CS, $y = 3.152x - 0.414$; $r^2 = 0.448$). (b) Manus basin (CS, $y = 1.299x - 0.131$; $r^2 = 0.951$). (c) East Scotia ridge segments E2–E4 (CS, $y = 3.171x - 0.238$; $r^2 = 0.796$) and E5–E8. (d) East Scotia ridge segment E9 (CS, $y = 1.106x - 0.098$; $r^2 = 0.831$). (e) Southern Lau basin Valu Fa ridge (VFR) and the eastern Lau spreading center (ELSC) segments (CS, $y = 3.450x - 0.265$; $r^2 = 0.910$); note the difference between DMM and CS models in this region. (f) Northern Lau basin central Lau spreading center (CLSC), intermediate Lau spreading center (ILSC), and Mangatolu triple junction (MTJ) segments (CS, $y = 1.524x - 0.119$; $r^2 = 0.710$). Note one ESR-E9 point and one Manus point highlighted with dark circles and arrows, which were excluded from modeling because they likely degassed. Arrows indicate the direction these points would shift had they not degassed. Data sources are given in the text, and details for each region are given in the auxiliary material.

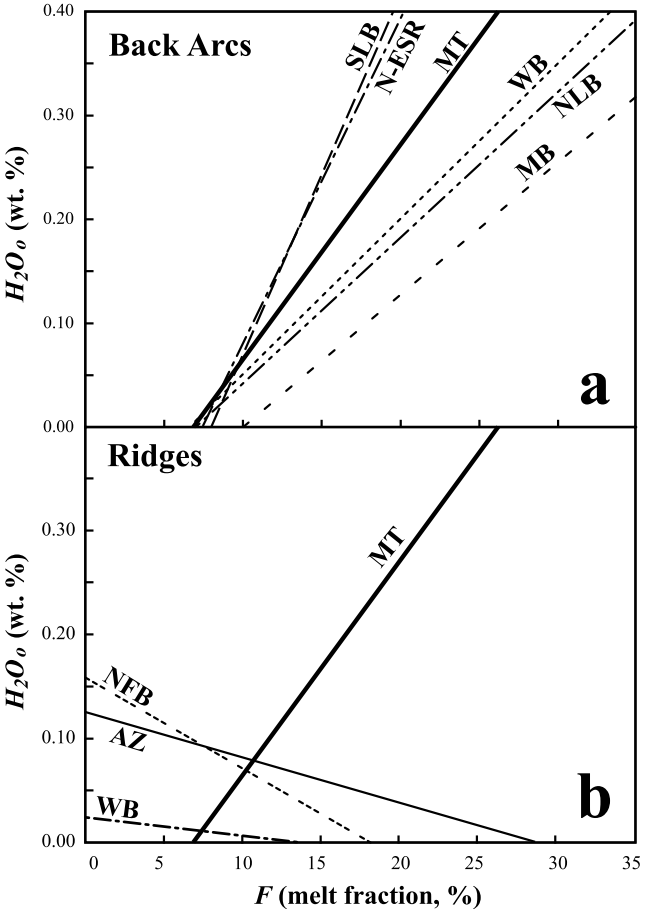


**Figure 11.** Compilation of $H_2O_o$ versus $F$ best fits for mid-ocean ridges and back-arc basins. (a) Results for back-arc basins, showing trends with positive, variable slopes at East Scotia ridge segments E2–E4 (N-ESR), the southern Lau basin (SLB), the Woodlark basin (WB), the Sumisu rift (SR), the Manus basin (MB), and the northern Lau basin (NLB). (b) Results for mid-ocean ridges, showing trends with negative slopes at the North Fiji basin (NFB), wet samples from the Azores platform region of the Mid-Atlantic Ridge (AZ), and dry samples from the Woodlark basin (WB). The Mariana trough (MT) from Figure 11a is shown for reference. In both panels, all lines shown are for regressions through CS results (as distinguished in Figures 10 and 12).

that increasing $F$ correlates with increasing $H_2O$. Using the fractionation corrections and melting model developed here, we find that the maximum $H_2O$ concentrations in both the lavas and the mantle at back-arc basins far exceed those at mid-ocean ridges, and the principal relationship between $H_2O_o$ and $F$ is positive (Figure 10). Mantle $H_2O$ concentrations at back arcs range from MORB-like values (0.01–0.05 wt %), which are present at all basins, to maxima of 0.4–0.5 wt % $H_2O$ at the Manus basin and the Valu Fa ridge. Positive trends in $H_2O_o$ versus $F$ vary regionally in slope and intercept (Table 4), with the East Scotia ridge segments E2–E4 and the southern Lau basin defining the steepest trends and the Manus and northern Lau basins the shallowest (Figure 11a). The calculated $F$ is <20% in most samples from all back-arc basins, with only a few extreme samples indicating $F > 20\%$. Correcting for mantle source depletion has the largest effect for the Valu Fa ridge, where the mantle is the most depleted relative to DMM (Figure 10e). All arrays defined by back-arc basins indicate finite melt fraction at zero (or low) $H_2O_o$, which strongly implicates decompression melting if we accept that melting in the absence of a flux agent like $H_2O$ must be generated by adiabatic decompression. However, the important point in our view is the robust and recurring positive relationship between $H_2O$ and extent of melting at back-arc basins.

[29] The negatively sloping relationship between $H_2O_o$ and $F$ proposed for mid-ocean ridges by *Asimow and Langmuir* [2003] and *Cushman et al.* [2004] is apparent at four regions (Figure 12): two mid-ocean ridges (GSC, Azores platform), and two spreading centers with distant or past associations with subduction (N. Fiji basin, Woodlark basin). In these regions, melt fraction broadly decreases as a function of increasing $H_2O_o$, although these relationships are much weaker than for back arcs. Maximum $H_2O_o$ concentrations reached at these places are low (max. 0.08 wt % $H_2O_o$ (Figure 12)) compared to active back-arc basins, and are well within the storage capacity of $H_2O$ in nominally anhydrous upper mantle phases such as olivine, orthopyroxene, and clinopyroxene (e.g., 0.12–0.38 wt % $H_2O$ at 3 GPa [*Hirschmann et al.*, 2005]). The negatively sloped trends in $H_2O_o$ versus $F$ observed at classic mid-ocean ridges (Azores, GSC) are in regions of ridge–hot spot interaction, where constraints on mantle source variation are essential for successful modeling (and, indeed, $TiO_2$ and $H_2O$ generally vary with isotope ratios). We are not fully satisfied with any of the approaches for quantifying chemical source variations of the mantle in these regions (including the approach based on $TiO_2$/Y ratios presented here), and consequently the significance of these negative slopes is uncertain. We conclude, however, that such negative slopes are indeed real phenomena, given their persistence at two of three ridges regardless of which approach is taken to constrain variations in source composition and the appearance of such a trend at part of the Woodlark basin. This basic difference in the character of the trend of $H_2O_o$ versus $F$ at mid-ocean ridges versus back-arc basins suggests to us a fundamental difference in the role of $H_2O$ in the melting processes beneath back arcs and mid-ocean ridges.

## 4. Discussion

### 4.1. Effects of Variable Mantle Temperature

[30] Constraining mantle temperature variations beneath back-arc basins is important for understanding subduction zone petrogenesis, structure, and evolution. The 150°C temperature range calculated here (i.e., 1350°–1500°C (Figure 2, Table 4)), using only the driest back-arc basalts, is within the range of global MORBs, which sample upper mantle that spans a ~250°C range in $T_p$ [*Klein and Langmuir*, 1987; *McKenzie and Bickle*, 1988; *Langmuir et al.*, 1992]. Back arcs thus appear to sample mantle of similar temperature to mid-ocean ridges, reflecting normal thermal variations in the upper mantle. The high-$T$ end of the MORB range, however, is due largely to hot spot proximity (e.g., the Mid-Atlantic Ridge in the vicinity of

Iceland). Such a hot spot influence at back-arc basins seems unlikely since the slab would generally shield the overlying mantle wedge from the thermal effects of deep upwelling plumes. At the northern segments of the Lau basin, however, infiltration of the Samoan mantle plume through a tear in the subducting plate has been proposed to account for along-strike geochemical variations [*Poreda and Craig*, 1992] and this could have thermal consequences as well. Among the back-arc basins considered here, the Manus basin taps mantle of the highest $T_p$; geochemical evidence such as high $^3He/^4He$ ratios [*Shaw et al.*, 2004] is also consistent with a hot spot contribution to this elevated $T_p$. The mantle temperatures calculated by us for back-arc basins also correlate with variations in the *S* wave velocity structure of mantle beneath four back-arc basins at 40–100 km depth [*Wiens et al.*, 2006]. Specifically, the *S* wave velocities decrease with increasing temperature, with the Mariana trough as the coldest/fastest and the northern Lau basin as the hottest/slowest, strongly supporting our determination of significant thermal variations in these settings.

[31] Although back-arc basin basalts thus appear similar to MORBs with respect to mantle $T_p$, our results demonstrate they are quite different in that they have much higher $H_2O_o$ concentrations (approaching 0.5 wt % in some cases) and define positive, linear trends in $H_2O_o$ versus *F*. Moreover, the variations in slope correlate with the $T_p$ variations described above based on independent measures ($Na_2O$ and FeO). The relationship between slope ($dF/dH_2O_o$, an expression of wet melt productivity) and temperature (Figure 13) is not an unexpected result, since isothermal-isobaric models predict this effect [S&N94; *Hirose and Kawamoto*, 1995; G&G98; *Hirschmann et al.*, 1999; *Reiners et al.*, 2000; *Katz et al.*, 2003]. On the basis of our results, melt productivities in the sources of back-arc basin magmas increase from ~30 to 80%/wt % (i.e., % *F* per wt % $H_2O_o$) as $T_p$ increases by 150°C; this result is similar to those of MELTS calculations, which predict wet

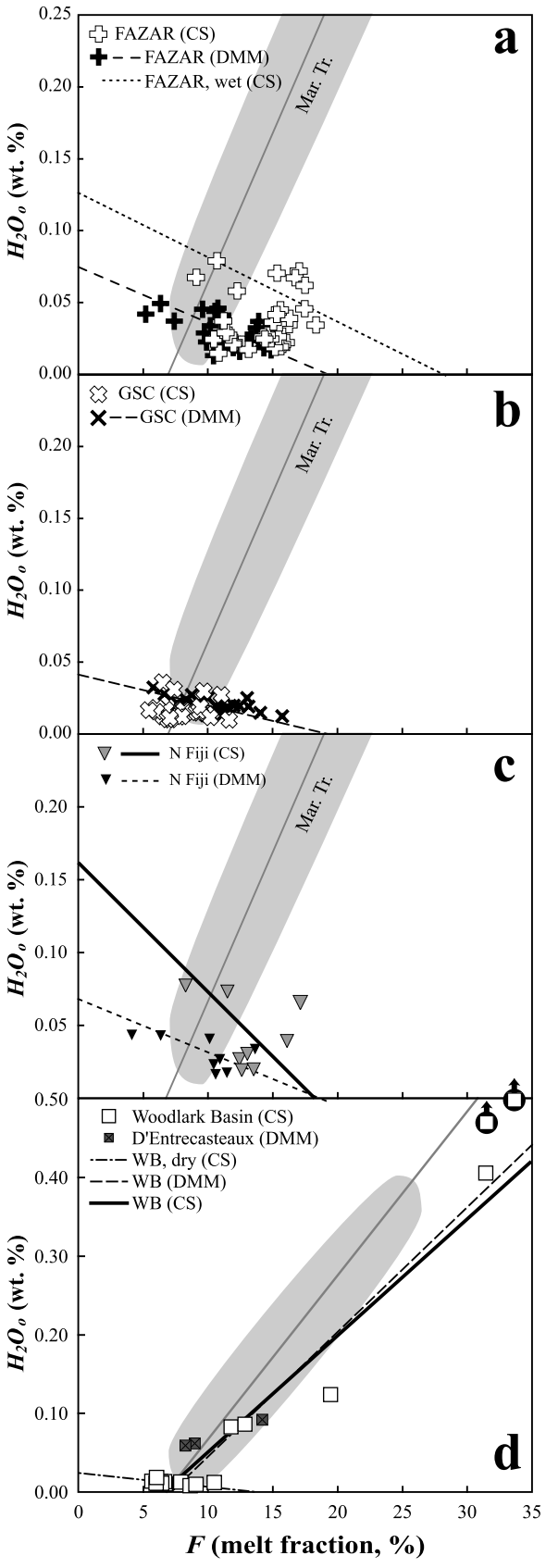


**Figure 12.** $H_2O_o$ versus *F* at mid-ocean ridges and spreading centers distant from subduction zones. The shaded region shows part or all of the range of Mariana trough data from Figure 9b, and the line through the shaded region shows the best fit line. As in Figure 10, model results using a constant MORB mantle source are labeled DMM ($C^o_{Ti}$ = 0.133); results using variable mantle source constraints modeled in this work are labeled CS (corrected source; $C^o_{Ti}$ given in Table 1). (a) Mid-Atlantic Ridge and Azores platform (FAZAR) (DMM, $y = -0.390x + 0.075$; $r^2 = 0.229$); the CS results here indicate a negatively sloped trend for the 10 wet samples from the Azores platform (wet CS, $y = -0.447x + 0.128$; $r^2 = 0.0823$) that may be distinct from the rest of the ridge, which is comparatively dry and alone does not produce a resolvable trend. (b) Galápagos spreading center (GSC) (DMM, $y = -0.214x + 0.040$; $r^2 = 0.284$); note that the CS results do not produce a resolvable trend. (c) North Fiji basin (CS, $y = -0.886x + 0.163$; $r^2 = 0.069$). (d) Woodlark basin (WB), which shows two distinct, oppositely sloping trends in the wet (all CS, $y = 1.482x - 0.097$; $r^2 = 0.923$) and dry samples (dry CS, $y = -0.173x + 0.025$; $r^2 = 0.106$). Note two WB model points highlighted with dark circles and arrows, which were excluded from modeling because they likely degassed some $H_2O$. Arrows indicate the direction these points would shift had they not degassed. Data sources are given in the text, and details for each region are given in the auxiliary material.

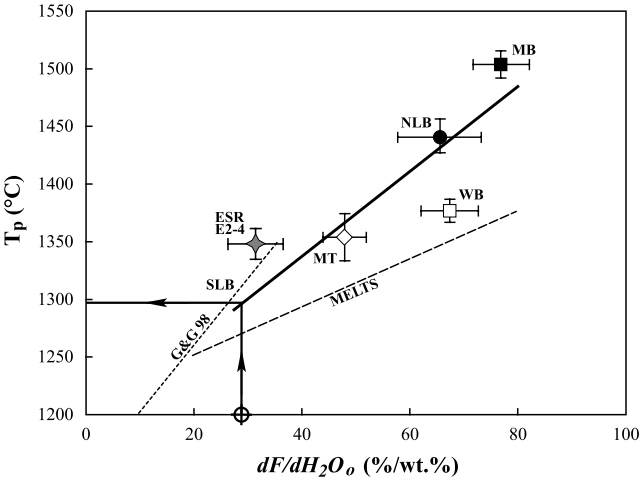


**Figure 13.** Mantle potential temperature ($T_p$) from Figure 2 versus wet melt productivity ($dF/dH_2O_o$) from Figure 11 at back-arc basins (values given in Table 4). $T_p$ is constrained from dry glasses from each basin (<0.5 wt % $H_2O$), whereas $dF/dH_2O_o$ is constrained using wet and dry samples as shown in Figures 10–12. Regions shown are the large-scale basin averages for the Manus basin (MB; solid square), the northern Lau basin (NLB; solid circle), the Woodlark basin (WB; open square), the Mariana trough (MT; open diamond), and the East Scotia ridge (ESR; shaded star) segments E2–E4. Error bars for $dF/dH_2O_o$ are the standard error on the linear regression, and error bars for $T_p$ are 1σ deviations from the regional, basin-scale averages (Table 4). The solid black line is a linear regression through these points ($y = 368.6x + 1191$; $r^2 = 0.66$). The southern Lau basin (SLB) is shown as a crossed circle on the $x$ axis because this region illustrates how measured wet melt productivity may be used to constrain $T_p$ in places where $T_p$ cannot be independently determined through Na-Fe systematics. The long-dashed line is the range of wet melt productivities from *Hirschmann et al.* [1999] (MELTS), and the short-dashed line is the trend of wet melt productivities from G&G98.

melt productivities of 20–80%/wt % over a 125°C temperature range, although offset to lower absolute temperatures and pressure (1250°–1375°C at 1 GPa [*Hirschmann et al.*, 1999]; see Figure 13). The experimental results of G&G98 indicate melt productivities generally lower than those we have inferred (10–36%/wt % at 1200°–1350°C and 1.5 GPa; see Figure 13) but they overlap with our empirical trend at ~1300°C.

[32] The correlation between $dF/dH_2O_o$ and $T_p$ has the potential to provide an alternative approach to estimating mantle $T_p$; this would be particularly useful for regions with $H_2O$ concentrations too high to permit successful modeling of Na and Fe variations, in regions at which variations in source composition lead to deviations from the global MORB trend in Fe-Na, and for volcanic arc fronts [*Kelley et al.*, 2003]. At the Valu Fa ridge (VFR), for example, water contents of erupted glasses and melt inclusions do not overlap with MORB, and the relationship between Na and Fe in these samples is disrupted by uniformly high $H_2O$. Samples from the VFR do, however, form a steep linear trend in $H_2O_o$ versus $F$ (Figure 12e), indicating less efficient melt productivity, which is consistent with cooler mantle $T_p$ beneath the VFR than the northern Lau basin (Figure 13) and suggests an along-strike thermal gradient in the Lau basin. In principle, the $F$-intercept of the trend could also provide constraints on mantle $T_p$, but high errors on the intercept relative to the slope make $dF/dH_2O_o$ a more robust indicator.

[33] Additional factors related to mantle temperature beneath back-arc basins include cooling from the subducting plate, convergence rate, and back-arc spreading rate [e.g., *Peacock*, 1996; *Kincaid and Sacks*, 1997; *Kincaid and Hall*, 2003; *England and Wilkins*, 2004], and the calculated mantle temperatures for various back-arc basins based on our results can be used to evaluate the effects of these various factors on $T_p$. For example, in the Lau basin, distance from the spreading axis to the trench (and slab) decreases toward the south (Figure 14), and this may be partially responsible for cooler $T_p$ at the VFR relative to the northern basin. Likewise, convergence rate and back-arc spreading rate are thought to be linked, since fast subduc-

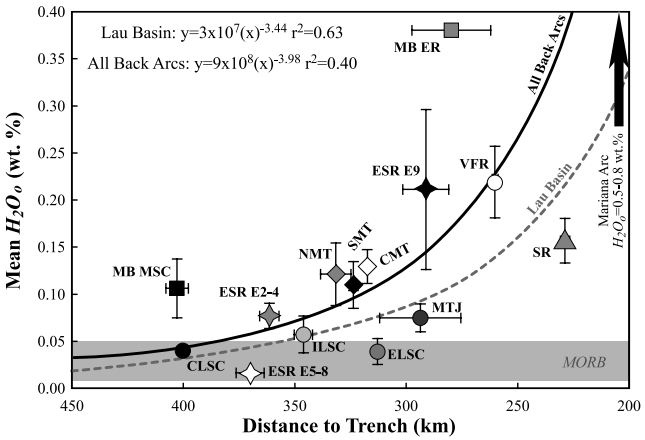


**Figure 14.** Mean $H_2O_o$ versus distance to the trench at back-arc basins (values given in Table 4). The back-arc basin data are regional averages of the Manus basin Eastern Rifts (MB ER; shaded square) and the Manus spreading center/eastern transform zone (MB MSC; solid square), the Lau basin central Lau spreading center (CLSC; solid circle), the intermediate Lau spreading center (ILSC; light shaded circle), the Mangatolu triple junction (MTJ; dark shaded circle), the eastern Lau spreading center (ELSC; medium shaded circle) and the Valu Fa ridge (VFR; open circle), the East Scotia ridge (ESR) segments E2–E4 (shaded star), E5–E8 (open star), and E9 (solid star), and the Mariana trough northern third (NMT, 19°N–21°N; shaded diamond), central third (CMT, 17°N–19°N, open diamond) and southern third (SMT 15°N–17°N, solid diamond). Error bars are 1σ deviations from the small-scale averages (Table 4). The shaded field is the range of $H_2O_o$ in MORB from this study (Figure 12). The black arrow in the upper right indicates the direction that volcanic arcs are predicted to plot (off-scale). The range for the Mariana arc is from *Kelley et al.* [2003]. The dashed shaded curve is a power law regression through the five Lau basin segment averages. The solid black curve is a power law regression through all of the back-arc segments shown.

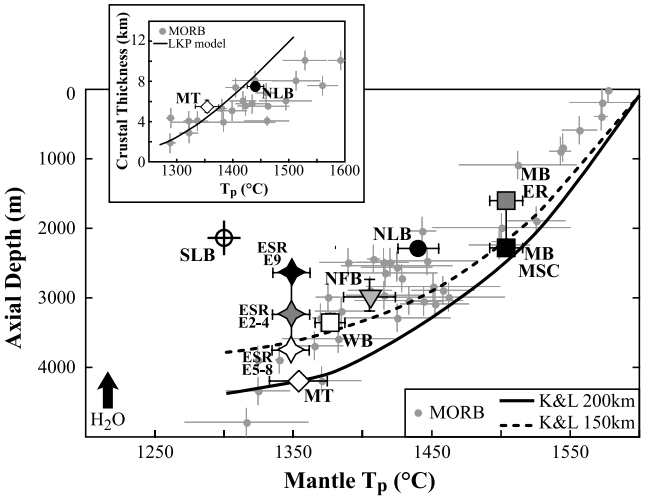


**Figure 15.** Mantle potential temperature ($T_p$) versus axial depth at back-arc basins. Shaded circles are MORB from *Langmuir et al.* [1992], with $T_p$ as calculated here (equations (12) and (13) in text; see also Figure 2). The back-arc basin data are regional averages of the Manus basin Eastern rift (MB ER; shaded square) and Manus spreading center (MB MSC; black square) segments, the northern Lau basin (NLB, black circle), the North Fiji basin (NFB, inverted shaded triangle), the Woodlark basin (WB, open square), the East Scotia ridge segments E2–E4 (ESR E2–4, shaded star), E5–E8 (ESR E5–8, open star) and E9 (ESR E9, black star), and the Mariana trough (open diamond). Error bars are 1σ deviations from the basin-scale or small-scale averages (Table 4). The southern Lau basin (SLB) is shown as a crossed circle at the $T_p$ indicated by Figure 13. The solid curve is the model from *Klein and Langmuir* [1987] for 200 km compensation depth; the dashed curve is for 150 km compensation depth. Inset shows $T_p$ versus crustal thickness; the solid line is the model curve from *Langmuir et al.* [1992]. The black arrow in the lower left indicates the direction that $H_2O$ addition to the mantle should drive axial depth and crustal thickness. Extra melting from $H_2O$ should create more crust and shallower axial depth than a dry ridge at the same $T_p$.

tion is expected to drive more rapid wedge circulation and back-arc mantle upwelling, and the fast back-arc spreading will in turn lead to increased relative convergence between the overriding and subducting plates. Our results are consistent with these expectations: convergence rates are fast at the Tonga/Lau and New Britain/Manus (>140 mm/yr) subduction zones, where back-arc temperatures are warmer, and slow at the Mariana (40–70 mm/yr) and South Sandwich/East Scotia (67–79 mm/yr) subduction zones [*Taylor and Martinez*, 2003, and references therein], where back-arc $T_p$ is cooler.

[34] An important test of the wet melt productivities calculated here is the effect on the volume of crust created, as recorded in crustal thickness or axial depth (e.g., Figure 15). Extents of melting at back-arc spreading centers are driven higher than MORB by the addition of $H_2O$, and high extents of melting should result in thick crust and shallow axial depth relative to mid-ocean ridges. Axial depth at back arcs varies from ~1900 to 4300 meters below sea level, within the range of mid-ocean ridges. Geochemical indicators of extent of mantle melting, such as $Na_{8.0}$, broadly correlate with axial depth at back arcs, as at ridges (Figure 1 [see also *Klein and Langmuir*, 1987]), although regions with shallow axial depth and high $H_2O_o$ (e.g., the southern Lau basin and the Manus basin (Figure 1b, open symbols)) tend to have lower mean $Na_{8.0}$ than ridges of the same depth. In comparison to the driest melts from each region ($H_2O$ < 0.5 wt % (Figure 1b, solid symbols)), however, average back-arc melts (Figure 1b, open symbols) are skewed to low $Na_{8.0}$ (esp. basins where mean $H_2O_o$ is high; Mariana, Manus, southern Lau basins), consistent with high $H_2O$ driving higher $F$ and lower $Na_{8.0}$ (Table 3, Figure 1b).

[35] We may also compare back-arc mantle $T_p$ and axial depth to that of ridges, which show a positive relationship owing to the greater thermal buoyancy, compositional buoyancy, and crustal thickness of hotter regions (Figure 15 [see also *Klein and Langmuir*, 1987]). We find that most back-arc spreading axes are at water depths consistent with their mantle temperatures, suggesting that the excess melt produced by high $H_2O$ leads to small shifts in axial depth, generally within the range of ridges. For the Mariana trough and the northern Lau basin, the two basins with constraints on both crustal thickness and mantle $T_p$, we also find that back-arc basins are within the range of normal mid-ocean ridges, albeit plotting toward the high crustal thickness side of the ridge array (Figure 15, inset). Mantle temperature thus appears to be the dominant physical variable contributing to melt generation beneath many back-arc basins. On the other hand, clear excess melt production is present for the most water-rich back-arc segments, where anomalously shallow axial depth results from the excess melt produced by $H_2O$ addition (see SLB, NLB, ESR E2-4/E9 and MB ER points in Figure 15). Thus water clearly contributes excess melt production in the wettest regions, whereas lavas from other regions may only reflect high extents of melting of small mantle source volumes and preferentially erupt wet melts.

### 4.2. Effects of Variable Mantle $H_2O$ Concentration

[36] The $H_2O_o$ concentrations at mid-ocean ridges, with few exceptions, do not exceed 0.01–0.05 wt % (max. $H_2O_o$ = 0.08 wt % at the Azores platform), which is well below the minimum storage capacity of $H_2O$ in nominally anhydrous mantle phases at pressures near the onset of melting (i.e., 0.12 wt % $H_2O$ at 3 GPa [*Hirschmann et al.*, 2005]). On the basis of our results, however, the sources of back-arc basin basalts have $H_2O_o$ concentrations of 0.01–0.50 wt % (and possibly higher when considering degassed samples (Figure 10)). In many regions, these concentrations clearly locally exceed the minimum storage capacity of nominally anhydrous mantle minerals (i.e., 0.18 wt % $H_2O$ at 6 GPa [*Hirschmann et al.*, 2005]). We do note that *Hirschmann et al.* [2005] report a large range of permissible mantle $H_2O$ storage capacities (0.18–0.63 wt % at 6 GPa) and their preferred model indicates a storage capacity of 0.44 wt% $H_2O$ at 6 GPa, which would only be exceeded by the wettest local regions indicated by our study. We emphasize, however, that many regions locally exceed the minimum storage capacity, and back-arc basin mantle

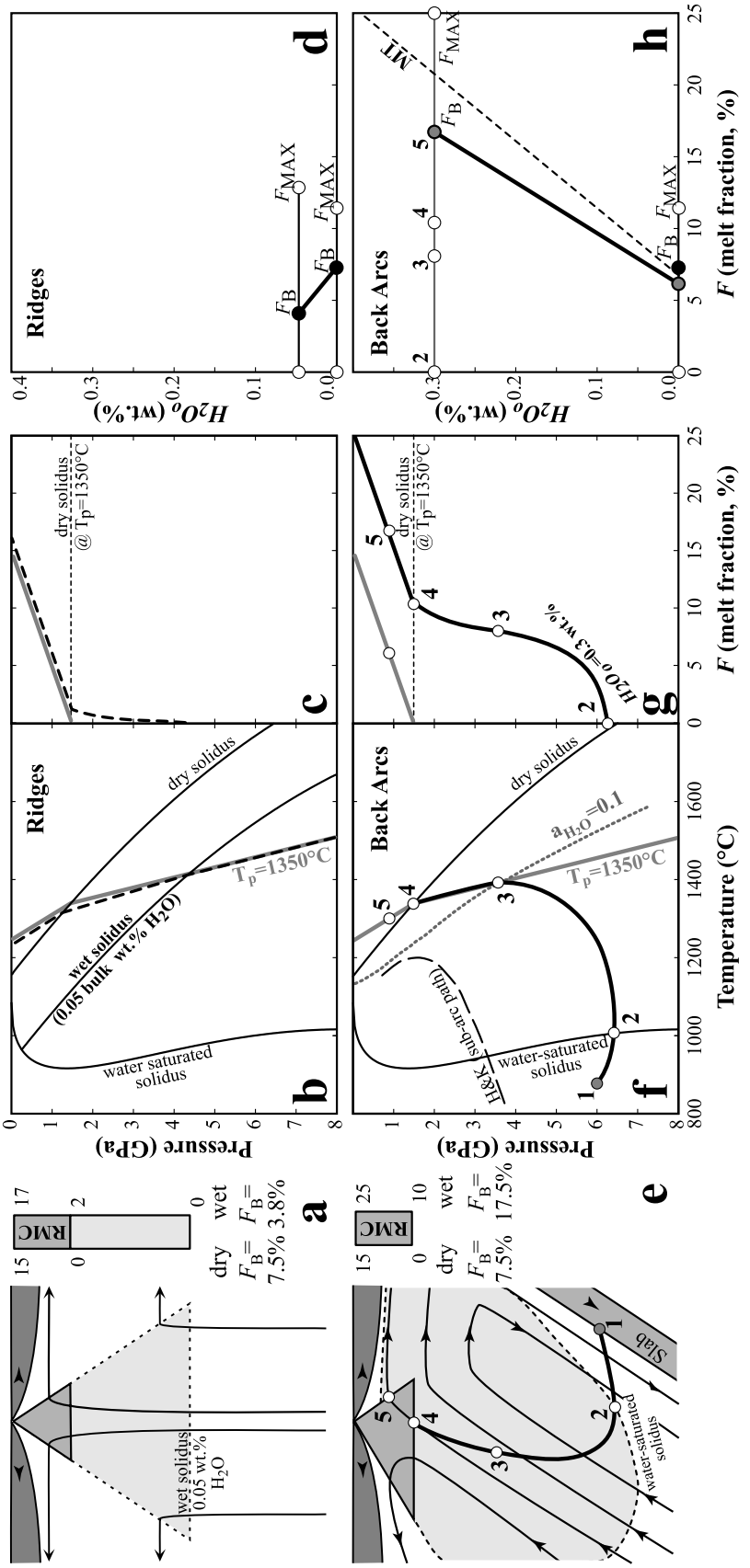
a
RMC
wet solidus
0.05 wt.%
H2O
dry
wet
FB= FB=
7.5% 3.8%
e
RMC
dry
wet
FB= FB=
7.5% 17.5%
Slab
water-saturated
solidus
b
Ridges
dry solidus
Tp=1350°C
wet solidus
(0.05 bulk wt.% H2O)
water saturated
solidus
Pressure (GPa)
c
dry solidus
@ Tp=1350°C
d
Ridges
FB
FMAX
H2Oo (wt.%)
f
Back Arcs
dry solidus
aH2O=0.1
Tp=1350°C
H&K
sub-arc path
water-saturated
solidus
Pressure (GPa)
Temperature (°C)
g
dry solidus
@ Tp=1350°C
H2Oo=0.3 wt.%
h
Back Arcs
MIT
FB
FMAX
H2Oo (wt.%)
F (melt fraction, %)

Figure 16

sources may thus contain some $H_2O$ in excess of the nominally anhydrous minerals. As shown in Figure 14, water concentrations in back-arc mantle tend to increase as spreading axes approach the trench. The wettest spreading segments (e.g., Valu Fa, Manus ER, East Scotia E9, Sumisu) are located ~300 km or less from the trench. Figure 14 shows some back-arc mantle $H_2O$ in excess of average MORB up to 400 km from the trench, but the average $H_2O_o$ concentrations increase rapidly (fit by a power law) as trench distance decreases below ~300 km. There is also evidence of even higher $H_2O_o$ values beneath the Mariana arc (Figure 14 [*Kelley et al.*, 2003]), suggesting that the trenchward increase in $H_2O_o$ defined by back-arc basins may extend to the mantle beneath arcs. At the other extreme, the North Fiji basin has an average $H_2O_o$ similar to MORB (0.05 wt % (Table 4)) and is ~800 km east of the New Hebrides/Vanuatu trench. The distance to the trench in this case is consistent with the low mantle $H_2O$ concentrations, and is clearly too far for this ridge to incorporate direct $H_2O$ additions from the slab. These relationships strongly suggest that the subducting slab is the ultimate source of elevated $H_2O$ at back arcs, as well as at arcs, and provide observational constraints on how $H_2O$ may be lost from the slab and transported through the mantle wedge.

### 4.3. Different Roles of $H_2O$ at Ridges and Back-Arc Basins

[37] On the basis of our results, there appears to be a distinction between basalts from mid-ocean ridges (and spreading centers distant from subduction zones), where increasing $H_2O$ is accompanied by decreasing extents of melting (i.e., $dF/dH_2O_o < 0$), and basalts from back-arc basins, where high $H_2O$ is associated with high extents of melting (i.e., $dF/dH_2O_o > 0$). How can we explain the different behavior of ridges and back-arc basins during wet melting? Although there are many possibilities, we focus here on the hypothesis that the contrasting trends relate to the relative concentrations of $H_2O$ in the two environments. At ridges, water is present in low concentrations, likely dissolved in solid, nominally anhydrous phases such as olivine and pyroxene prior to melting. As such, the shape of the melting regime, and the production of melts and their mixing proportions, are governed to first order by decompression paths along the solid flow field [*Langmuir et al.*, 1992]. At back arcs, on the other hand, $H_2O$ added from the subducting plate will, according to our results, at least locally exceed the nominal storage capacity of the mantle. In such cases, excess $H_2O$ is supplied to the mantle melting region via fluids or melts, driving high degrees of melting in a process that may be independent of the solid flow field of the mantle. In this final section, we develop these ideas further, and explore some of the consequences of this hypothesis. Figures 16 and 17 portray the different processes that contribute to melting beneath mid-ocean ridges and back-arc basins. Note that these scaled cartoons are designed to be more illustrative than exclusive.

#### 4.3.1. A Back-Arc Melting Model

[38] In the mantle wedge above subduction zones, *P-T* conditions experienced by ascending $H_2O$, melt and mantle are unlikely to be adiabatic in the classic sense, in contrast to the conditions beneath a ridge (Figure 16). In particular, the thermal gradient above the slab is influenced by heat flow from the mantle wedge into the cold slab, so as water released from the slab (and any subsequent melt) ascends to lower pressure, its temperature increases as it migrates away from the cold slab and into the warm interior of the mantle

**Figure 16.** Contrasting *P*, *T*, *F*, and $H_2O_o$ relationships for mid-ocean ridges and back-arc basins. (a) Scaled cartoon and residual mantle column (RMC). (b) Pressure versus temperature phase diagram and (c) pressure versus *F*, illustrating the melting mechanism responsible for (d) decreasing bulk *F* with increasing $H_2O_o$ at mid-ocean ridges (after *Asimow and Langmuir* [2003]). In Figure 16b the dry solidus is from *Langmuir et al.* [1992]; the wet solidi are from *Katz et al.* [2003]; the heavy, solid shaded line is an adiabatic path for anhydrous mantle of $T_p$ = 1350°C; the long-dashed black line is an adiabatic path for hydrous mantle ($H_2O_o$ = 0.05 wt %). In Figure 16c the solid shaded line is *F* along the anhydrous, adiabatic path, and the long-dashed black line is *F* along the hydrous, adiabatic path, showing how mantle intersects the solidus deeper in the wet case than the dry case, but the wet mantle experiences only low extents of melting before reaching the dry solidus. In Figure 16d the integrated mean *F* over the full pressure range of melting ($F_B$) in the wet case is less than in the dry case despite reaching a higher maximum *F*. (e) Scaled cartoon and residual mantle column (RMC), (f) pressure versus temperature phase diagram, and (g) pressure versus *F*, illustrating the melting mechanism responsible for (h) increasing bulk *F* with increasing $H_2O_o$ beneath back-arc basins. In Figure 16e the bold line illustrates one possible path that $H_2O$ may follow from the slab through the mantle, with numbered points corresponding to the points in Figures 16f–16h. Water leaves the slab and enters the mantle at point (1), wet melting initiates at point (2), the ascending melt ± mantle achieve an adiabatic path at point (3), dry melting initiates at point (4), and melting ceases at point (5). The mantle flow lines and the asymmetric melting triangle in Figure 16e are based on the back-arc mantle flow geometry of *Conder et al.* [2002]. In Figure 16f the phase boundaries and the dry adiabat are identical to Figure 16b, and the bold line is the path of $H_2O$ through the mantle wedge as in Figure 16e, increasing in temperature with decreasing pressure until intersecting and following the adiabatic path. The dotted shaded line is the schematically located $H_2O$ activity ($a_{H2O}$) of 0.1 (after *Hirth and Kohlstedt* [1996]), and the long-dashed black curve (Figure 16f, labeled H&K) is the path of intermediate-rate, networked flow of hydrated mantle ascending beneath an arc, from *Hall and Kincaid* [2001]. In Figure 16g the solid shaded line is *F* along the anhydrous, adiabatic path as in Figure 16c, and the bold numbered curve shows possible melt production from $H_2O$ addition along the path in Figures 16e–16f for a $H_2O_o$ concentration of 0.3 wt %. High wet melt productivities are achieved along the path of increasing *T* (see text). In Figure 16h, melt fractions achieved by each numbered point are shown along a line of constant $H_2O_o$ (0.3 wt %), illustrating how $H_2O$ addition drives bulk *F* ($F_B$) and maximum *F* ($F_{MAX}$) higher than in the dry case. The series of $F_B$ points corresponding to $H_2O_o$ from 0 to 0.3 wt % (not shown) would produce a positive $H_2O_o$-*F* trend similar to the Mariana trough (MT, dashed line).

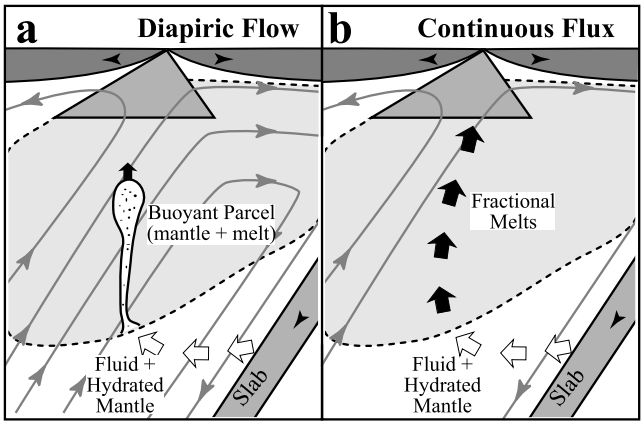


**Figure 17.** Cartoon illustrating possible melting mechanisms beneath back-arc basins. (a) Diapiric flow of buoyant mantle through the wedge [*Davies and Stevenson*, 1992; *Hall and Kincaid*, 2001; *Gerya and Yuen*, 2003]. Mantle and melt ascend together as a buoyant parcel above the wet solidus. (b) Continuous fluxing of $H_2O$ from the slab through the mantle wedge. Fractional melts form at the wet solidus, rapidly separate from the mantle source, and ascend through the dry melting regime. If solid mantle flow is slow compared to the rate of $H_2O$ flux, continuous addition of $H_2O$ from the slab will progressively melt a single mantle volume.

wedge (Figure 16e, point 1 [*Baker et al.*, 1994; *Hall and Kincaid*, 2001; *Grove et al.*, 2002]). Melting under such conditions may also be described as adiabatic if heat is conserved within the system and the ascending material cools as it ascends. However, if the volumes of fluid and melt are small relative to the heat reservoir of the mantle wedge, the impact of $H_2O$ transport and melting on the heat budget of the system may be negligible and the early stages of melting may thus be nonadiabatic. Melting initiates once the mobilized $H_2O$ crosses the $H_2O$-saturated solidus in the mantle wedge (Figure 16e, point 2). Under the conditions proposed here near the initiation of melting (high pressure and a free $H_2O$-rich fluid phase), the fluid in the $H_2O$-silicate system could instead be supercritical, in which case the concept of $H_2O$-saturated melting would not apply at the earliest stages of melting [*Shen and Keppler*, 1997; *Mibe et al.*, 2004]. Constraints on the supercritical behavior of basaltic melts and aqueous fluids, however, are still in their infancy and we therefore elect to describe the initiation of melting relative to the $H_2O$-saturated solidus even at these high pressures. The nature of the melt migration process through the mantle wedge is not well known. Reactive porous flow of the $H_2O$-rich melt through the mantle is the most likely mechanism [*Davies and Stevenson*, 1992; G&G98], but melt and mantle could ascend together as a buoyantly unstable parcel that upwells beneath the arc and back arc (Figure 17a [*Davies and Stevenson*, 1992; *Hall and Kincaid*, 2001; *Gerya and Yuen*, 2003]). The buoyant parcel may follow a path similar to that for diapiric networked flow described by *Hall and Kincaid* [2001], which exchanges heat as it traverses the hot interior of the mantle wedge. Eventually, the parcel becomes entrained in the adiabatically upwelling paths beneath the back arc (Figure 16e, point 3) that cross the dry solidus (Figure 16e, point 4) and melt further due to adiabatic decompression.

[39] Other reasonable physical models involve separation of melt and solid flow. If melting is a fractional process, the melt and the mantle will not ascend together as a single parcel. Melt will instead become separated from its mantle source, drawing $H_2O$ with it and preventing further $H_2O$-fluxed melting of the mantle source from taking place. In this case, however, if the mantle is resupplied and remelted by a continuous flux of $H_2O$ from the slab, then the final pooled melt will reflect the integrated, fractional melting of a single mantle source (Figure 17b). This fractional process would produce melt compositions similar to the final melt of the batch process described above [*Plank and Langmuir*, 1992]. In this case, the continuous flux of $H_2O$ and melt through a single mantle volume could imitate melting under isobaric, isothermal conditions, provided the process is nonadiabatic as described above, since each increment of the $H_2O$/melt flux experiences a similar set of conditions along a path through the mantle wedge. Reactive transport of melt through the mantle wedge [e.g., *Kelemen et al.*, 1997] might also create the appropriate $H_2O$-$TiO_2$ relationships, but quantitative models require better constraints on melt versus solid flow vectors in the mantle wedge.

[40] The resulting melt fraction, as recorded by the $TiO_2$ concentration of the ascending melt, along the path through the mantle wedge (as illustrated in Figure 16) may be estimated with some simple approximations, borrowing from the melting models developed by *Hirth and Kohlstedt* [1996] and *Katz et al.* [2003]. Consider mantle with 0.3 wt % $H_2O_o$ (near the high end of the back arc spectrum). This water is supplied from the subducting plate, and drives melting in the mantle at the water-saturated solidus (Figures 16e–16f, point 2). The initial $H_2O$ concentration of this melt is high (e.g., ~30 wt % $H_2O$ [*Grove et al.*, 2002]), but the melt $H_2O$ concentration is continually diluted as melting proceeds. When the parcel reaches pt. 3 in Figure 16e, the activity of $H_2O$ in the melt ($a_{H2O}$) is 0.1, or 10% of saturation (note that the activity curve is schematically located in Figure 16e [*Hirth and Kohlstedt*, 1996]), and so the $H_2O$ concentration of the melt will now be ~3.5 wt % ($H_2O$ sat. = 35% at 4.3 GPa [*Katz et al.*, 2003]). Since melting began in a mantle with $H_2O_o$ = 0.3 wt %, we use equation (10) to determine that the melt at pt. 3 reflects ~8% melting of this mantle (in contrast to a ridge case where, for $H_2O_o$ = 0.05 wt %, the amount of melt at this same point reflects only $F$ = 0.04%). As the melting path becomes vertical and mantle parcels ascend adiabatically, melting continues as convective adiabatic decompression melting, with the bulk composition of the source fixed such that $H_2O$ concentration (and activity) in the partial melt decrease progressively. Melt productivity in the ascending mantle will continually decrease because the $H_2O$ content of the melt is diluted as melting proceeds, moving the effective solidus to progressively higher temperatures. In any case, we assume that melt generation above point 4 occurs at a rate similar to dry systems (~1% melt per kilobar of ascent), attaining maximum, final melt fractions in excess of 20% [see also *Gaetani and Grove*, 2003]. The melting path thus reflects a combination of wet, nonadiabatic and wet, adiabatic melting (Figure 16e).

#### 4.3.2. Breakdown of the Melting Regime "Shape" Control

[41] The driest back-arc basin magmas are more comparable to the mid-ocean ridge environment, where relatively dry mantle undergoes melting largely above the dry solidus, to an extent controlled by mantle $T_p$. Such compositions define the $F$-intercept of the wet melting trends characteristic of both back-arc basins and ridges (Figures 16d and 16h). When the water content of the mantle is low enough that all the water can be accommodated in nominally anhydrous mantle phases, melting is "organized" by the 2-D triangular shape of the melting regime, and provided all the melt from the triangle can be pooled, leads to a $F$ versus $H_2O_o$ trend with a negative slope [*Asimow and Langmuir*, 2003; *Cushman et al.*, 2004]. Beneath back-arc basins, the water content is large enough that significant melting takes place at depths well below those at which the shape of the melting regime has any meaning, leading to a quantitatively different set of controls on the extent of melting. Back-arc basins achieve a positive vector of increasing $F$ with increasing $H_2O_o$ because high-$F$, wet melting paths contribute large $F$ before entering the triangular melting regime (Figures 16e–16g). In the ridge case, bulk $F$ is dominated by the large source volume of low $F$, wet melts. In the back-arc case, the bulk $F$ is dominated by high $F$, wet melts.

[42] The unique geometry of plate and mantle juxtaposition at subduction zones also leads to a number of dynamical consequences for both the shape of the melting regime and the interpretation of erupted melt compositions. We examine, for example, the relationship between $H_2O$ and melt regime volume. At mid-ocean ridge settings, where $H_2O$ is present as a trace element dissolved in solid mantle minerals, the pooling of melt within the triangle leads to a decrease in bulk melt fraction with increasing $H_2O_o$ (e.g., Figure 16d [*Asimow and Langmuir*, 2003]). Water in such a system increases the depth at which adiabatically upwelling mantle intersects the solidus ($P_o$), allowing the production of low-degree, wet melts within the ascending mantle before intersecting the dry solidus (Figures 16a–16d). Increasing $H_2O_o$ in this system increases both $P_o$ and the volume of the low-$F$, wet melting region. For the maximum $H_2O_o$ in MORB ($\sim$500 ppm), wet melting begins at $\sim$4.5 GPa ($\sim$150 km (Figure 16a)). This large, low-$F$, wet-melt volume below the base of the dry-melt triangle skews the bulk melt fraction over the full melting region to much lower values.

[43] Beneath back-arc basins, however, this relationship may not be so simple. In these settings, the initial depth of melting may be controlled by the water-saturated solidus, which is independent of the normal controls on melting regime shape imposed by mantle $T_p$, plate spreading, and passive corner flow as at ridges. The addition of water to back-arc mantle does allow a larger mantle volume to experience partial melting than at a dry ridge (Figure 16g), but increasing the flux of $H_2O$ into the mantle does not necessarily increase the volume of the wet melting regime. Instead, an increased flux of water effectively breaks the control of the melting regime shape on the depth and extent of melting, allowing for higher extents of melting of the same mantle volume. In this view, $F$ increases with increasing $H_2O_o$. Because $H_2O_o$ increases toward the trench (i.e., $H_2O_o$ is higher at shallower depths), melting will also take place at progressively shallower depths, although the amount of $H_2O$ that can be dissolved in melt at these lower pressures is much less. The depth of melting thus may, in fact, decrease as $H_2O_o$ increases in the mantle wedge.

[44] Another dynamical consequence of subduction zone geometry relates to melt focusing and pooling. Mid-ocean ridge magmas reflect the bulk melt fraction ($F_B$ [*Plank et al.*, 1995]) removed from mantle passing through the wide melting region beneath the ridge, but back-arc melts may be biased toward the maximum melt fraction ($F_{MAX}$). Melt focusing and pooling across the melting regime is an efficient process beneath ridges. Mantle flow beneath back arcs, however, is perturbed by wedge circulation, which deflects flow toward the wedge corner and the slab [*Spiegelman and McKenzie*, 1987; *Conder et al.*, 2002; *Kincaid and Hall*, 2003]. This geometry could lead to preferential focusing of low-$F$ melts from the slab side of the melting triangle into the magmatic plumbing system beneath the arc. The effect of such a process would lead to a preferential increase in the bulk $F$ recorded by melts erupted at back arcs, and the magnitude would scale with proximity to the slab, which controls wedge circulation and $H_2O_o$ concentration. The active flux of water to the back-arc melting region may also lead to lower viscosity melts that pool more vertically, or even organize flow into vertical instabilities (Figure 17). Thus such melts may not blend as efficiently across the melting region as at ridges. In such a case, the range of lava compositions erupted at back arcs might be greater than at ridges, and we would expect to find dry and wet melts locally erupted, as is the case in the Mariana trough. Alternatively, the positive $H_2O_o$-$F$ trend could instead reflect binary mixing of separate melts from a dry, MORB melting regime and a high-$F$, wet melting regime, although in this case the initial mantle source composition could be different for each melting end-member. In order to further evaluate the distribution and relative importance of wet and dry melts and their mantle sources on local and regional scales, however, more data are required for more densely sampled back-arc regions.

[45] The positive relationships between $H_2O_o$ and $F$ at back-arc basins derive from several consequences of an active supply of water from the subducting plate. (1) Water concentrations in excess of the minimum solid mantle storage capacity (>0.18 wt %) suggest the presence of free fluid or melt along a significant portion of the back-arc mantle path, rather than incorporation of $H_2O$ in solid flow as is thought to be the case at ridges. (2) Because of the inverted thermal gradient imposed by the cold subducting plate, and the small volume of initial melts relative to the mantle, the deepest parts of the melting paths beneath back arcs may not be adiabatic. (3) Melt production beneath back arcs is not governed solely by the shape of the melting regime generated by the solid flow field, but also by the magnitude of the $H_2O$ flux from the slab. (4) The extent of lateral pooling beneath back arcs may be less than at ridges, leading to a dominance of vertical pooling and strong local vectors of variability.

## 5. Conclusions

[46] The compiled data and calculations presented here confirm the unique role of $H_2O$ in the mantle melting process beneath back-arc basins. The first-order observation

of negatively sloping correlations between $H_2O$ and $TiO_2$ in erupted back-arc basin basalts suggests a relationship between $H_2O$ and extent of melting, since $TiO_2$ is incompatible during melting and is conservative within the subduction zone (i.e., all $TiO_2$ in the magmas is assumed to come from the mantle wedge, not from the slab). Using $TiO_2$ to calculate the mantle melt fraction ($F$) reveals positive, linear correlations between $H_2O$ addition from the slab and $F$ beneath back-arc basins the world over, but with slopes and intercepts that vary regionally. The positive wet melting functions at back arcs contrast with what is observed at mid-ocean ridges, where increasing mantle $H_2O$ contents correlate with decreasing $F$. We conclude that back-arc mantle temperature varies regionally by $\sim$150°C and plays an important role in melt production in a manner similar to mid-ocean ridges, largely controlling physical variables such as axial depth and crustal thickness, as well as wet melt productivity ($dF/dH_2O_o$). Superimposed on temperature is the effect of $H_2O$ on melt production, as high $H_2O_o$ correlates positively with high $F$. The concentration of $H_2O_o$ varies in the back-arc mantle as a function of distance from the trench and relates to the orientation (+ or −) of wet melting trends modeled at back-arc basins and mid-ocean ridges. We infer that the presence of the subducting slab in close proximity to back-arc spreading centers initiates a critical change in the role of water during melting, from a relatively passive participant in adiabatic melt generation beneath mid-ocean ridges, to an active fluxing agent that drives melt generation in the back-arc environment.

[60] **Acknowledgments.** Many thanks to M. Hirschmann, R. Katz, C. Langmuir, D. Wiens, B. Taylor, A. Kent, J. Sinton, P. Asimow, G. Hirth, and P. Kelemen for sharing results, unpublished data, and discussion, which were all critical to the successful completion of this study. We also thank E. Klein, J. Dixon, and an anonymous reviewer for careful, thoughtful, and thorough reviews. This work was funded by support from NSF OCE-0001897 and the NSF MARGINS Program as well as by an NSF graduate research fellowship. Development and writing of this manuscript was also supported by a Carnegie Postdoctoral Fellowship.

## References

Aggrey, K. E., D. W. Muenow, and J. M. Sinton (1988), Volatile abundances in submarine glasses from the North Fiji and Lau back-arc basins, *Geochim. Cosmochim. Acta*, *52*, 2501–2506.

Ambos, E. L., and D. M. Hussong (1982), Crustal structure of the Mariana Trough, *J. Geophys. Res.*, *87*, 4003–4018.

Anderson, A. T., Jr. (1979), Water in some hypersthenic magmas, *J. Geol.*, *87*, 509–531.

Anderson, A. T., Jr. (1982), Parental basalts in subduction zones: Implications for continental evolution, *J. Geophys. Res.*, *87*, 7047–7060.

Asimow, P. D., and C. H. Langmuir (2003), The importance of water to oceanic mantle melting regimes, *Nature*, *421*, 815–820.

Asimow, P. D., M. M. Hirschmann, and E. M. Stolper (2001), Calculation of peridotite partial melting from thermodynamic models of minerals and melts; IV, Adiabatic decompression and the composition and mean properties of mid-ocean ridge basalts, *J. Petrol.*, *42*, 963–998.

Asimow, P. D., J. E. Dixon, and C. H. Langmuir (2004), A hydrous melting and fractionation model for mid-ocean ridge basalts: Application to the Mid-Atlantic Ridge near the Azores, *Geochem. Geophys. Geosyst.*, *5*, Q01E16, doi:10.1029/2003GC000568.

Aubaud, C., E. H. Hauri, and M. M. Hirschmann (2004), Hydrogen partition coefficients between nominally anhydrous minerals and basaltic melts, *Geophys. Res. Lett.*, *31*, L20611, doi:10.1029/2004GL021341.

Baker, M. B., T. L. Grove, and R. Price (1994), Primitive basalts and andesites from the Mt. Shasta region, N. California: Products of varying melt fraction and water content, *Contrib. Mineral. Petrol.*, *118*, 111–129.

Baker, M. B., M. M. Hirschmann, M. S. Ghiorso, and E. Stolper (1995), Compositions of near-solidus peridotite melts from experiments and thermodynamic calculation, *Nature*, *375*, 308–311.

Bartels, K. S., R. J. Kinzler, and T. L. Grove (1991), High pressure phase relations of primitive high-alumina basalts from Medicine Lake Volcano, Northern California, *Contrib. Mineral. Petrol.*, *108*, 253–270.

Bender, J. F., C. H. Langmuir, and G. N. Hanson (1984), Petrogenesis of basalt glasses from the Tamayo region, East Pacific rise, *J. Petrol.*, *25*, 213–254.

Bibee, L. D., G. G. Shor, and R. S. Lu (1980), Inter-arc spreading in the Mariana Trough, *Mar. Geol.*, *35*, 183–197.

Cervantes, P., and P. J. Wallace (2003), Role of $H_2O$ in subduction-zone magmatism: New insights from melt inclusions in high-Mg basalts from central Mexico, *Geology*, *31*, 235–238.

Conder, J. A., D. A. Wiens, and J. Morris (2002), On the decompression melting structure at volcanic arcs and back-arc spreading centers, *Geophys. Res. Lett.*, *29*(15), 1727, doi:10.1029/2002GL015390.

Crawford, W. C., J. A. Hildebrand, L. M. Dorman, S. C. Webb, and D. A. Wiens (2003), Tonga Ridge and Lau Basin crustal structure from seismic refraction data, *J. Geophys. Res.*, *108*(B4), 2195, doi:10.1029/2001JB001435.

Cushman, B., J. Sinton, G. Ito, and J. Eaby Dixon (2004), Glass compositions, plume-ridge interaction, and hydrous melting along the Galápagos Spreading Center, 90.5°W to 98°W, *Geochem. Geophys. Geosyst.*, *5*, Q08E17, doi:10.1029/2004GC000709.

Danyushevsky, L. V., T. J. Falloon, A. V. Sobolev, A. J. Crawford, M. Carroll, and R. C. Price (1993), The $H_2O$ content of basalt glasses from southwest Pacific back-arc basins, *Earth Planet. Sci. Lett.*, *117*, 347–362.

Davies, J. H., and D. J. Stevenson (1992), Physical model of source region of subduction zone volcanics, *J. Geophys. Res.*, *97*, 2037–2070.

Detrick, R. S., J. M. Sinton, G. Ito, J. P. Canales, M. Behn, T. Blacic, B. Cushman, J. E. Dixon, D. W. Graham, and J. J. Mahoney (2002), Correlated geophysical, geochemical, and volcanological manifestations of plume-ridge interaction along the Galápagos Spreading Center, *Geochem. Geophys. Geosyst.*, *3*(10), 8501, doi:10.1029/2002GC000350.

Devey, C. W., D. Garbe-Schönberg, P. Stoffers, C. Chauvel, and D. F. Mertz (1994), Geochemical effects of dynamic melting beneath ridges: Reconciling major and trace element variations in Kolbeinsey (and global) mid-ocean ridge basalt, *J. Geophys. Res.*, *99*, 9077–9095.

Dixon, J. E., and E. Stolper (1995), An experimental study of water and carbon dioxide solubilities in mid-ocean ridge basaltic liquids. part II. Applications to degassing, *J. Petrol.*, *36*, 1633–1646.

Dixon, J. E., E. Stolper, and J. R. Holloway (1995), An experimental study of water and carbon dioxide solubilities in mid-ocean ridge basaltic liquids. part I: Calibration and solubility models, *J. Petrol.*, *36*, 1607–1631.

Dixon, J. E., L. Leist, C. H. Langmuir, and J.-G. Schilling (2002), Recycled dehydrated lithosphere observed in plume-influenced mid-ocean-ridge basalt, *Nature*, *420*, 385–389.

Dosso, L., H. Bougault, C. H. Langmuir, C. Bollinger, O. Bonnier, and J. Etoubleau (1999), The age and distribution of mantle heterogeneity along the Mid-Atlantic Ridge (31–41°N), *Earth Planet. Sci. Lett.*, *170*, 269–286.

Dril, S. I., M. I. Kuzmin, S. S. Tsipukova, and L. P. Zonenshain (1997), Geochemistry of basalts from the western Woodlark, Lau and Manus basins: Implications for the petrogenesis and source rock compositions, *Mar. Geol.*, *142*, 57–83.

Eiler, J. M., A. Crawford, T. Elliott, K. A. Farley, J. W. Valley, and E. Stolper (2000), Oxygen isotope geochemistry of oceanic-arc lavas, *J. Petrol.*, *41*, 229–256.

Eissen, J.-P., M. Nohara, J. Cotten, and K. Hirose (1994), North Fiji Basin basalts and their magma source: part I. Incompatible element constraints, *Mar. Geol.*, *116*, 153–178.

England, P., and C. Wilkins (2004), A simple analytical approximation to the temperature structure in subduction zones, *Geophys. J. Int.*, *159*, 1138–1154, doi:10.1111/j.1365-246X.2004.02419.x.

Fretzdorff, S., R. A. Livermore, C. W. Devey, P. T. Leat, and P. Stoffers (2002), Petrogenesis of the back-arc East Scotia Ridge, South Atlantic Ocean, *J. Petrol.*, *43*, 1435–1467.

Gaetani, G. A., and T. L. Grove (1998), The influence of water on melting of mantle peridotite, *Contrib. Mineral. Petrol.*, *131*, 246–323.

Gaetani, G. A., and T. L. Grove (2003), Experimental constraints on melt generation in the mantle wedge, in *Inside the Subduction Factory*, *Geophys. Monogr. Ser.*, vol. 138, edited by J. M. Eiler, pp. 107–134, AGU, Washington, DC.

Gaetani, G. A., T. L. Grove, and W. B. Bryan (1994), The influence of water on the petrogenesis of subduction related igneous rocks, *Nature*, *365*, 332–335, doi:10.1038/365332a0.

Gerya, T. V., and D. A. Yuen (2003), Rayleigh-Taylor instabilities from hydration and melting propel "cold plumes" at subduction zones, *Earth Planet. Sci. Lett.*, *212*, 47–62.

Gill, J. B. (1981), *Orogenic Andesites and Plate Tectonics*, 390 pp., Springer, New York.

Gribble, R. F., R. J. Stern, S. H. Bloomer, D. Stuben, T. O'Hearn, and S. Newman (1996), MORB mantle and subduction components interact to generate basalts in the southern Mariana Trough back-arc basin, *Geochim. Cosmochim. Acta*, *60*, 2153–2166.

Gribble, R. F., R. J. Stern, S. Newman, S. H. Bloomer, and T. O'Hearn (1998), Chemical and isotopic composition of lavas from the northern Mariana Trough: Implications for magmagenesis in back-arc basins, *J. Petrol.*, *39*, 125–154.

Grove, T. L., S. W. Parman, S. A. Bowring, R. C. Price, and M. B. Baker (2002), The role of an $H_2O$-rich fluid component in the generation of primitive basaltic andesites and andesites from the Mt. Shasta region, N California, *Contrib. Mineral. Petrol.*, *142*, 375–396.

Hall, P. S., and C. Kincaid (2001), Diapiric flow at subduction zones: A recipe for rapid transport, *Science*, *292*, 2472–2475.

Hauri, E. H., G. A. Gaetani, and T. H. Green (2006), Partitioning of water during melting of the upper mantle sources of oceanic basalts, *Earth Planet. Sci. Lett.*, in press.

Hawkins, J. W., P. F. Lonsdale, J. D. Macdougall, and A. M. Volpe (1990), Petrology of the axial ridge of the Mariana Trough backarc spreading center, *Earth Planet. Sci. Lett.*, *100*, 226–250.

Hirose, K., and T. Kawamoto (1995), Hydrous partial melting of lherzolite at 1 GPa: The effect of $H_2O$ on the genesis of basaltic magmas, *Earth Planet. Sci. Lett.*, *133*, 463–473.

Hirschmann, M. M., P. D. Asimow, M. S. Ghiorso, and E. Stolper (1999), Calculation of peridotite partial melting from thermodynamic models of minerals and melts. III. Controls on isobaric melt production and the effect of water on melt production, *J. Petrol.*, *40*, 831–851.

Hirschmann, M. M., C. Aubaud, and A. C. Withers (2005), Storage capacity of $H_2O$ in nominally anhydrous minerals in the upper mantle, *Earth Planet. Sci. Lett.*, *236*, 167–181, doi:10.1016/j.epsl.2005.04.022.

Hirth, G., and D. Kohlstedt (1996), Water in the oceanic upper mantle: Implications for rheology, melt extraction and the evolution of the lithosphere, *Earth Planet. Sci. Lett.*, *144*, 93–108.

Hochstaedter, A., J. B. Gill, M. Kusakabe, S. Newman, M. S. Pringle, B. Taylor, and P. Fryer (1990a), Volcanism in the Sumisu Rift, I. Major element, volatile, and stable isotope geochemistry, *Earth Planet. Sci. Lett.*, *100*, 179–194.

Hochstaedter, A., J. B. Gill, and J. D. Morris (1990b), Volcanism in the Sumisu Rift, II. Subduction and non-subduction related components, *Earth Planet. Sci. Lett.*, *100*, 195–209.

Kamenetsky, V. S., A. J. Crawford, S. Eggins, and R. Mühe (1997), Phenocryst and melt inclusion chemistry of near-axis seamounts, Valu Fa Ridge, Lau Basin: Insight into mantle wedge melting and the addition of subduction components, *Earth Planet. Sci. Lett.*, *151*, 205–223.

Kamenetsky, V. S., R. A. Binns, J. B. Gemmell, A. J. Crawford, T. P. Mernagh, R. Maas, and D. Steele (2001), Parental basaltic melts and fluids in eastern Manus backarc basin: Implications for hydrothermal mineralisation, *Earth Planet. Sci. Lett.*, *184*, 685–702.

Katz, R. F., M. Spiegelman, and C. H. Langmuir (2003), A new parameterization of hydrous mantle melting, *Geochem. Geophys. Geosyst.*, *4*(9), 1073, doi:10.1029/2002GC000433.

Kelemen, P. B., N. Shimizu, and T. Dunn (1993), Relative depletion of niobium in some arc magmas and the continental crust: Partitioning of K, Nb, La and Ce during melt/rock reaction in the upper mantle, *Earth Planet. Sci. Lett.*, *120*, 111–134.

Kelemen, P. B., G. Hirth, N. Shimizu, M. Spiegelman, and H. J. B. Dick (1997), A review of melt migration processes in the adiabatically upwelling mantle beneath mid-ocean ridges, *Philos. Trans. R. Soc. London, Ser. A*, *355*, 283–318.

Kelley, K. A., T. Plank, S. Newman, E. Stolper, T. L. Grove, S. Parman, and E. Hauri (2003), Mantle melting as a function of water content in arcs, *Eos Trans. AGU*, *84*(46), Fall Meet. Suppl., Abstract V41D-06.

Kent, A. J. R., D. W. Peate, S. Newman, E. Stolper, and J. A. Pearce (2002), Chlorine in submarine glasses from the Lau Basin: Seawater contamination and constraints on the composition of slab-derived fluids, *Earth Planet. Sci. Lett.*, *202*, 361–377.

Kincaid, C., and P. S. Hall (2003), Role of back arc spreading in circulation and melting at subduction zones, *J. Geophys. Res.*, *108*(B5), 2240, doi:10.1029/2001JB001174.

Kincaid, C., and I. S. Sacks (1997), Thermal and dynamical evolution of the upper mantle in subduction zones, *J. Geophys. Res.*, *102*, 12,295–12,315.

Kinzler, R. J. (1997), Melting of mantle peridotite at pressures approaching the spinel to garnet transition: Application to mid-ocean ridge basalt petrogenesis, *J. Geophys. Res.*, *102*, 853–874.

Kinzler, R. J., and T. L. Grove (1992), Primary magmas of mid-ocean ridge basalts: 1. Experiments and methods, *J. Geophys. Res.*, *97*, 6885–6906.

Klein, E. M., and C. H. Langmuir (1987), Global correlations of ocean ridge basalt chemistry with axial depth and crustal thickness, *J. Geophys. Res.*, *92*, 8089–8115.

Klein, E. M., C. H. Langmuir, and H. Staudigel (1991), Geochemistry of basalts from the southeast Indian Ridge, 115°E–138°E, *J. Geophys. Res.*, *96*, 2089–2107.

Kushiro, I., Y. Syono, and S. Akimoto (1968), Melting of a peridotite nodule at high pressures and high water pressures, *J. Geophys. Res.*, *73*, 6023–6029.

Langmuir, C. H., E. M. Klein, and T. Plank (1992), Petrological systematics of mid-ocean ridge basalts: Constraints on melt generation beneath ocean ridges, in *Mantle Flow and Melt Generation at Mid-Ocean Ridges*, *Geophys. Monogr. Ser.*, vol. 71, edited by J. P. Morgan et al., pp. 183–280, AGU, Washington, DC.

LaTraille, S. L., and D. M. Hussong (1980), Crustal structure across the Mariana island arc, in *The Tectonic and Geologic Evolution of Southeast Asian Seas and Islands*, *Geophys. Monogr. Ser.*, vol. 23, edited by D. E. Hayes, pp. 209–221, AGU, Washington, DC.

Leat, P. T., R. A. Livermore, I. L. Millar, and J. A. Pearce (2000), Magma supply in back-arc spreading centre segment E2, East Scotia Ridge, *J. Petrol.*, *41*, 845–866.

Martinez, F., and B. Taylor (2003), Controls on back-arc crustal accretion: Insights from the Lau, Manus and Mariana basins, in *Intra-Oceanic Subduction Systems: Tectonic and Magmatic Processes*, edited by R. D. Larter and P. T. Leat, pp. 19–54, Geological Society, London.

McKenzie, D., and M. J. Bickle (1988), The volume and composition of melt generated by extension of the lithosphere, *J. Petrol.*, *29*, 625–679.

Mibe, K., M. Kanzaki, T. Kawamoto, K. N. Matsukage, Y. Fei, and S. Ono (2004), Determination of the second critical end point in silicate-$H_2O$ systems using high-pressure and high-temperature X-ray radiography, *Geochim. Cosmochim. Acta*, *68*, 5189–5195, doi:10.1016/j.gca.2004.07.015.

Michael, P. (1988), The concentration, behavior and storage of $H_2O$ in the suboceanic upper mantle: Implications for mantle metasomatism, *Geochim. Cosmochim. Acta*, *52*, 555–566.

Miller, D. M., S. L. Goldstein, and C. H. Langmuir (1994), Cerium/lead and lead isotope ratios in arc magmas and the enrichment of lead in the continents, *Nature*, *368*, 514–519.

Morris, J. D., W. P. Leeman, and F. Tera (1990), The subducted component in island arc lavas: Constraints from B-Be isotopes and Be systematics, *Nature*, *344*, 31–36.

Muenow, D. W., N. W. K. Liu, M. O. Garcia, and A. D. Saunders (1980), Volatiles in submarine volcanic rocks from the spreading axis of the East Scotia Sea back-arc basin, *Earth Planet. Sci. Lett.*, *47*, 149–153.

Muenow, D. W., M. R. Perfit, and K. E. Aggrey (1991), Abundances of volatiles and genetic relationships among submarine basalts from the Woodlark Basin, southwest Pacific, *Geochim. Cosmochim. Acta*, *55*, 2231–2239.

Newman, S., and E. Stolper (1995), $H_2O$ and $CO_2$ in back-arc basin basalts from the Scotia Sea, paper presented at the Annual Meeting of the Geological Association of Canada, Victoria, B. C., Canada, May.

Newman, S., E. Stolper, and R. J. Stern (2000), $H_2O$ and $CO_2$ in magmas from the Mariana arc and back arc systems, *Geochem. Geophys. Geosyst.*, *1*, doi:10.1029/1999GC000027.

Niu, Y., and R. Batiza (1997), Trace element evidence from seamounts for recycled oceanic crust in the eastern Pacific mantle, *Earth Planet. Sci. Lett.*, *148*, 471–483.

Nohara, M., K. Hirose, J.-P. Eissen, T. Urabe, and M. Joshima (1994), The North Fiji Basin basalts and their magma sources: Part II. Sr-Nd isotopic and trace element constraints, *Mar. Geol.*, *116*, 179–195.

Peacock, S. M. (1996), Thermal and petrological structure of subduction zones, in *Subduction: Top to Bottom*, *Geophys. Monogr. Ser.*, vol. 96, edited by G. E. Bebout et al., pp. 119–133, AGU, Washington, DC.

Pearce, J., and I. J. Parkinson (1993), Trace element models for mantle melting: Application to volcanic arc petrogenesis, in *Magmatic Processes and Plate Tectonics*, edited by H. M. Prichard et al., *Geol. Soc. Spec. Publ.*, *76*, 373–403.

Pearce, J. A., M. Ernewein, S. H. Bloomer, L. M. Parson, B. J. Burton, and L. E. Johnson (1995), Geochemistry of Lau Basin volcanic rocks: Influence of ridge segmentation and arc proximity, in *Volcanism Associated With Extension at Consumed Plate Margins*, edited by J. L. Smellie, *Geol. Soc. Spec. Publ.*, *81*, 53–75.

Peate, D. W., T. F. Kokfelt, C. J. Hawkesworth, P. W. Van Calsteren, J. M. Hergt, and J. A. Pearce (2001), U-series isotope data on Lau Basin glasses: The role of subduction-related fluids during melt generation in back-arc basins, *J. Petrol.*, *42*, 1449–1470.

Plank, T., and C. H. Langmuir (1992), Effects of the melting regime on the composition of the oceanic crust, *J. Geophys. Res.*, *97*, 19,749–19,770.

Plank, T., and C. H. Langmuir (1993), Tracing trace elements from sediment to volcanic output at subduction zones, *Nature*, *362*, 739–742.

Plank, T., M. Spiegelman, C. H. Langmuir, and D. W. Forsyth (1995), The meaning of "mean F": Clarifying the mean extent of melting at ocean ridges, *J. Geophys. Res.*, *100*, 15,045–15,052.

Poreda, R. J., and H. Craig (1992), He and Sr isotopes in the Lau Basin mantle: Depleted and primitive mantle components, *Earth Planet. Sci. Lett.*, *113*, 487–493.

Price, R. C., A. K. Kennedy, M. Riggs-Sneeringer, and F. A. Frey (1986), Geochemistry of basalts from the Indian ocean triple junction: Implications for the generation and evolution of Indian Ocean ridge basalts, *Earth Planet. Sci. Lett.*, *78*, 379–396.

Reiners, P. W., P. E. Hammond, J. M. McKenna, and R. A. Duncan (2000), Young basalts of the central Washington Cascades, flux melting of the mantle, and trace element signatures of primary arc magmas, *Contrib. Mineral. Petrol.*, *138*, 249–264.

Roggensack, K., R. L. Hervig, S. B. McKnight, and S. N. Williams (1997), Explosive basaltic volcanism from Cerro Negro volcano: Influence of volatiles on eruptive style, *Science*, *277*, 1639–1642.

Ryerson, F. J., and E. B. Watson (1987), Rutile saturation in magmas: Implications for Ti-Nb-Ta depletion in island arc basalts, *Earth Planet. Sci. Lett.*, *86*, 225–239, doi:10.1016/0012-821X(87)90223-8.

Salters, V. J. M., and A. Stracke (2004), Composition of the depleted mantle, *Geochem. Geophys. Geosyst.*, *5*, Q05B07, doi:10.1029/2003GC000597.

Shaw, A. M., D. R. Hilton, C. G. Macpherson, and J. M. Sinton (2004), The $CO_2$-He-Ar-$H_2O$ systematics of the Manus back-arc basin: Resolving source composition from degassing and contamination effects, *Geochim. Cosmochim. Acta*, *68*, 1837–1856, doi:10.1016/j.gca.2003.10.015.

Shen, A. H., and H. Keppler (1997), Direct observation of complete miscibility in the albite-$H_2O$ system, *Nature*, *385*, 710–712.

Sinton, J. M., R. C. Price, K. T. M. Johnson, H. Staudigel, and A. Zindler (1993), Petrology and geochemistry of submarine lavas from the Lau and North Fiji backarc basins, in *Basin Formation, Ridge Crest Processes and Metallogenesis in the North Fiji Basin*, *Earth Sci. Ser.*, vol. 15, edited by L. W. Kroenke and J. V. Eads, pp. 119–135, Circum-Pac. Counc. For Energy and Miner. Resour., Houston, Tex.

Sinton, J. M., L. L. Ford, B. Chappell, and M. T. McCulloch (2003), Magma genesis and mantle heterogeneity in the Manus back-arc basin, Papua New Guinea, *J. Petrol.*, *44*, 159–195.

Sisson, T. W., and S. Bronto (1998), Evidence for pressure-release melting beneath magmatic arcs from basalt at Galunggung, Indonesia, *Nature*, *391*, 883–886.

Sisson, T. W., and T. L. Grove (1993a), Experimental investigations of the role of $H_2O$ in calc-alkaline differentiation and subduction zone magmatism, *Contrib. Mineral. Petrol.*, *113*, 143–166.

Sisson, T. W., and T. L. Grove (1993b), Temperatures and $H_2O$ contents of low MgO high-alumina basalts, *Contrib. Mineral. Petrol.*, *113*, 167–184.

Sisson, T. W., and G. D. Layne (1993), $H_2O$ in basalt and basaltic andesite glass inclusions from four subduction-related volcanoes, *Earth Planet. Sci. Lett.*, *117*, 619–635.

Spiegelman, M., and D. McKenzie (1987), Simple 2-D models for melt extraction at mid-ocean ridges and island arcs, *Earth Planet. Sci. Lett.*, *83*, 137–152.

Stolper, E., and S. Newman (1994), The role of water in the petrogenesis of Mariana trough magmas, *Earth Planet. Sci. Lett.*, *121*, 293–325.

Tatsumi, Y., M. Sakuyama, H. Fukuyama, and I. Kushiro (1983), Generation of arc basalt magmas and thermal structure of the mantle wedge in subduction zones, *J. Geophys. Res.*, *88*, 5815–5825.

Taylor, B., and F. Martinez (2003), Back-arc basin basalt systematics, *Earth Planet. Sci. Lett.*, *210*, 481–497.

Taylor, B., A. M. Goodliffe, and F. Martinez (1999), How continents break up: Insights from Papua New Guinea, *J. Geophys. Res.*, *104*, 7497–7512.

Tera, F., L. D. Brown, J. D. Morris, S. Sacks, J. Klein, and J. Middleton (1986), Sediment incorporation in island-arc magmas: Inference from $^{10}$Be, *Geochim. Cosmochim. Acta*, *50*, 535–550.

Turner, I. M., C. Pierce, and M. C. Sinha (1999), Seismic imaging of the axial region of the Valu Fa Ridge, Lau Basin—The accretionary processes of an intermediate back-arc spreading ridge, *Geophys. J. Int.*, *138*, 495–519.

Volpe, A. M., J. D. Macdougall, and J. W. Hawkins (1987), Mariana Trough basalts (MTB): Trace element and Sr-Nd isotopic evidence for mixing between MORB-like and Arc-like melts, *Earth Planet. Sci. Lett.*, *82*, 241–254.

Walker, J. A., K. Roggensack, L. C. Patino, B. I. Cameron, and M. Otoniel (2003), The water and trace element contents of melt inclusions across an active subduction zone, *Contrib. Mineral. Petrol.*, *146*, 62–77, doi:10.1007/s00410-003-0482-x.

Weaver, S. J., and C. H. Langmuir (1990), Calculation of phase equilibrium in mineral-melt systems, *Comput. Geosci.*, *16*, 1–19.

Wiens, D. A., K. A. Kelley, and T. Plank (2006), Mantle temperature variations beneath back-arc spreading centers, *Earth Planet. Sci. Lett.*, in press.

T. L. Grove, Department of Earth, Atmospheric and Planetary Sciences, Massachusetts Institute of Technology, 77 Massachusetts Avenue, Cambridge, MA 02139, USA.

E. Hauri, Department of Terrestrial Magnetism, Carnegie Institution of Washington, 5241 Broad Branch Road, Washington, DC 20015, USA.

K. A. Kelley, Graduate School of Oceanography, University of Rhode Island, Narragansett Bay Campus, Narragansett, RI 02882, USA. (kelley@gso.uri.edu)

S. Newman and E. M. Stolper, Division of Geological and Planetary Sciences, California Institute of Technology, 1200 East California Boulevard, Pasadena, CA 91125, USA.

T. Plank, Department of Earth Sciences, Boston University, 685 Commonwealth Avenue, Boston, MA 02215, USA.